Two-dimensional structures of self-assembled alkyl substituted polyphenylene dendrimers on graphite

DISSERTATION

zur Erlangung des Grades eines Doktors

der Naturwissenschaften

vorgelegt von

Dott.ssa Simona Loi

aus Macerata

eingereicht beim Fachbereich 8

der Universität-Gesamthochschule-Siegen

Siegen 2001

1. Gutachter: Prof. Dr. H.-J. Butt
2. Gutachter: Prof. Dr. A. Meixner
3. Mitglied der Promotionskommission: Prof. Dr. B. Wenclawiak

Datum der mündlichen Prüfung: 07.12.2001

Index

Introduction

One challenge in nanotechnology and nanofabrication is the creation of supramolecular materials in which the constituent units are highly ordered macromolecules. Small functional units are usually made using macroscopic techniques, such as electron beam lithography to form individual microscopic structures (*top-down approach*). The smaller the structures are, the more complex and expensive the lithographic techniques become. Alternatively, one can form larger units by a spontaneous assembly of molecules (*bottom-up approach*). Examples are the formation of micelles from surfactants or the formation of biological membranes from lipids. While in the top-down approach individual structures are made sequentially, in the bottom-up approach many similar units are made with little technological effort. Hence, the techniques are complementary and both will probably be used for the fabrication of functional units with dimensions below 100 nm. In both approaches, surface properties become important because of the increasing surface to volume ratio with decreasing size of the objects. Progress in nanotechnology is greatly assisted by development in microscopy. Compared to other investigation methods that help to explore the relation between the molecular structure and macroscopic properties, microscopy gives the most direct information. In practise, the utilisation and value of microscopes depends on their spatial resolution, the contrast and the imaging conditions.

Three major advancements in resolution have occurred since Hooke's discovery of the optical microscope in 1665 [1]. In 1873, Ernst Abbe established fundamental criteria for the resolution limit in optical light microscopy [2], which did not exceed the range of a couple of 100 nm even after the introduction of the confocal optical microscope [3]. The invention of the transmission electron microscope in 1933 by the Nobel Price in physics 1986 Ernst Ruska extended the resolution of microscopes to the nanometer scale [4]. Finally, scanning tunnelling microscopy, introduced by Binnig and Rohrer in 1981, made a breakthrough when atomic resolution images were reported for the first time [5]. STM became the first member of a new class of scanning probe microscopes (SPMs), which are based on a different principle than the optical and electron microscopy. Instead of lenses and electromagnetic waves, SPMs, as atomic force microscope (AFM) use a sharp probe which scans across the sample to sense different types of interactions with the sample surface. In addition to the lateral resolution, SPMs are capable of three-dimensional imaging of the

surface and can provide a topographic map of the sample. Owing to the new operation principle, SPMs show few limitations regarding imaging conditions. Sample preparation became easier compared to the electron microscope. The latter often required sample treatment such as etching for the transmission electron microscope and metal sputtering for the scanning electron microscope, while the SPMs can visualise the native structure of the surface. Moreover, SPMs can operate in different environment including air, liquid and vacuum; this was a considerable advantage which allowed in-situ observation of biological systems in their natural medium.

Several molecules are known to self-assemble on solid surfaces as highly ordered, regular structures. Examples are thiols or disulfides on gold [6-8] or several surfactants on silica, graphite, mica or gold [9-11]. In contrast, macromolecules usually do not form periodically ordered structures on surfaces. Only few exceptions are known [12-14]. For example, thin films of several block copolymers form regular structures after annealing or as a melt [15-20].

In this thesis I am going to show that polyphenylene dendrimers are able to form ordered structures on graphite. Dendrimers are ideal to study this process because they are monodisperse macromolecules with a well-defined shape and dimension. Moreover, thanks to their catalytic [21], binding [22] and optical [23] properties, self-assembled nanostructures of dendrimers have potential applications as chemical sensors [24] and photosensitive materials [25]. Different modes of adsorption of dendrimers on surfaces have been observed, depending on the molecular structure and on the interfacial forces. Most of the dendritic molecules possess flexible branches and on a surface the molecules can adopt shapes that are far from globular. The aim of this thesis is the characterization of self-assembled layers from alkyl substituted polyphenylene dendrimers. These dendrimers are expected to be shape persistent due to a very dense packing of benzene rings. Hence, the resulting macromolecule can be regarded as rigid nanoparticle carrying a variety of functional groups on the outer shell. Through AFM experiments, I am going to investigate the influence of the substrate on the three-dimensional structure of these dendrimers and to check their ability to form specific supramolecular arrays. The comprehension of the processes that rule the formation of ordered structures on a solid substrate could be a first step for the employment of these dendrimers as building blocks for functional materials.

The self-assembly of alkyl substituted polyphenylene dendrimers on graphite was analysed with an AFM. *Chapter 1* introduces the fundamentals of atomic force microscopy, with respect to force measurement and surfaces imaging. The basic ideas about dendrimer synthesis and their possible applications will be described as well. In *Chapter 2* the dendrimers utilized in this thesis will be listed and the method for the sample preparation will be explained. *Chapter 3* presents the experimental results of the thesis. In a first part of the chapter, the ordered structures of different dendrimers are described. Then, the structural modifications of the self-assembled layers with changing experimental conditions are presented. The results will be summarized and discussed in *Chapter 4*.

1 Fundamentals

1.1 Atomic Force Microscopy

The measurements of this thesis were done with an atomic force microscope (AFM). It was the first of the scanning probe microscopies which overcame the limitation of STM in imaging thin samples on electrically conductive materials. In addition to the favourable imaging conditions and the high resolution, AFM offers the possibility to characterise mechanical properties and forces of the samples on the nanometer scale.

The five essential components of an AFM are: a sharp tip mounted on a soft cantilever spring; a way of sensing the cantilever's deflection; a feedback electronic system; a display system that converts the measured data into an image; a mechanical scanning system. In Figure 1.1a the probe, the scanner and the optical detection method are outlined. The tip (that part which directly interacts with the sample) is mounted on the cantilever. The cantilever is deflected by forces between the tip and the sample. The cantilevers deflection is detected and converted into an electronic signal that is utilized to reconstruct an image of the surface. One of the most utilised methods to detect the cantilever deflections is the *optical method*: it consists in focusing a laser beam on the back of the cantilever and measuring the displacements of the reflected beam on a multiple segment photodiode. The corresponding signals are acquired and processed by a feedback electronic. The feedback system is used to control the cantilever deflection and to direct consequently the piezoelectric scanner movements (see also Sect. 1.3). Usually, the tip is stationary while the sample is mounted onto a piezoelectric translator that moves the sample in the x, y and z directions under the tip. This configuration is easier to construct and allows for very precise control of the distances between tip and sample compared to a moving tip and a stationary sample.

One advantage of the AFM is that is the possibility to investigate the sample in liquid ambient (Figure 1.1b). In this way, for example, biologic samples can be imaged in physiological solution, i.e. in their natural environment. Generally, AFM imaging in liquids turns out to provide images of higher quality compared to imaging in air.

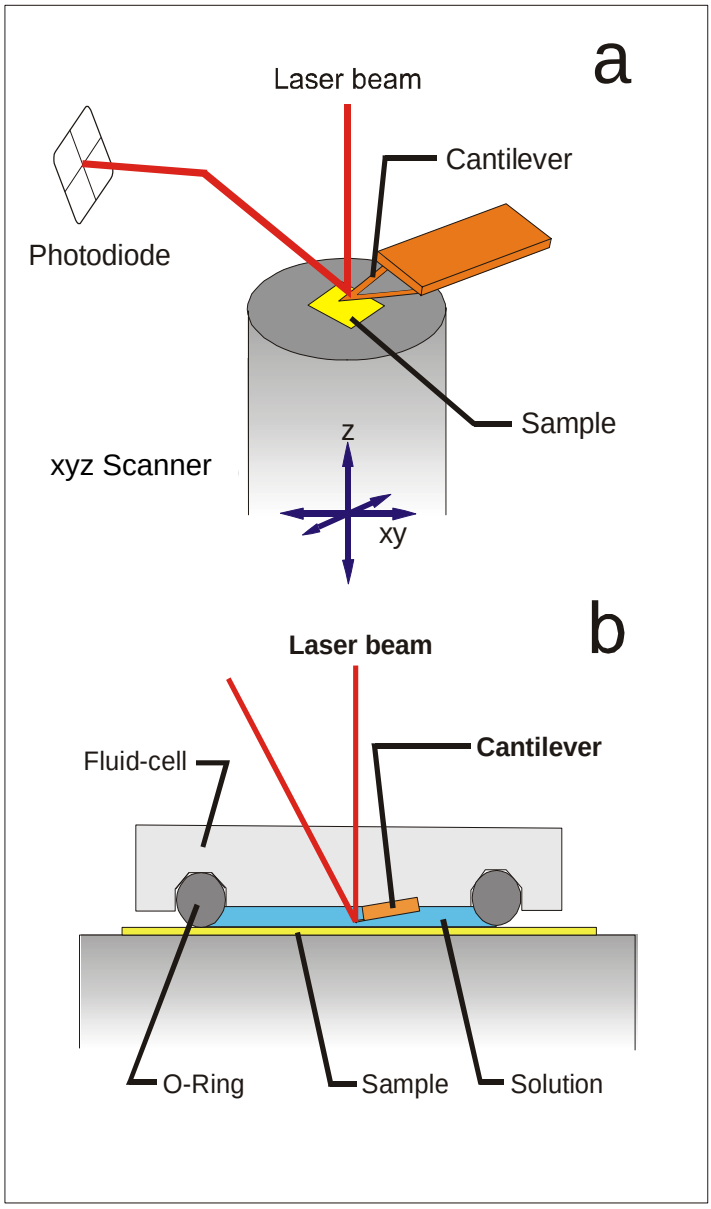

Figure 1.1: (a) Schematic representation of an AFM. The cantilever is fixed to a silicon-nitride microchip. At the end of the cantilever, on the side towards the sample, a pyramidal tip is attached. The tip is brought in to contact with the sample by a piezoelectric scanner in x, y and z direction. On the back of the cantilever a laser beam is focused and reflected on a photodiode. During a scan, the cantilever deflections due to surface height variations are monitored to obtain the surface topography. Different colours in the image correspond to different height values. (b) Cross section of the system for a measurement in liquid. The silicon-nitride microchip with the cantilever is fixed on the bottom side of a quartz glass cell. It is placed in the centre of a circular track, sealed with a silicon ring. The space between the fluid cell and the sample is filled with the solution.

During imaging the tip scans over a certain area of the sample, whereas forces are measured by approaching and withdrawing the tip over one point of the sample surface and plotting the cantilever deflection Z_c as a function of the vertical distance between tip and sample Z_s. The force acting on the cantilever is calculated from the product of the cantilever spring constant k and the cantilever deflection Z_c. One obtains two plots (for the approach and the withdrawal), the so-called *force-distance curves* (Figure 1.2). Each curve is characterised by a *zero line* and a *contact line*. In the approaching region, when tip and sample are still far away from each other, the cantilever is at the equilibrium position and the detected force is zero (*zero line*). On further approach, the cantilever will be deflected by the surface forces. At a certain distance one can observes an abruptly jump of the tip onto the sample surface that corresponds to a point of discontinuity in the force-curve (*snap-in*). This occurs if the gradient of the attractive forces becomes bigger than the sum of the elastic constant and of the gradient of repulsive forces. When the distance is further decreased, the tip is pressed against the sample (*contact line*) until a user defined force value is reached. At this point, the direction of the sample motion is inverted and the tip is withdrew from the sample. At a certain distance the tip detaches from the sample (*snap-out*) and the cantilever comes back to its equilibrium position. A zero force is acquired again (*zero line*). AFM can measure forces from pN to nN. During the approach, surface forces can be measured; the force corresponding to the *snap-out* is equal to the adhesion force between tip and sample. The slope of the *contact line* provides information on the sample stiffness.

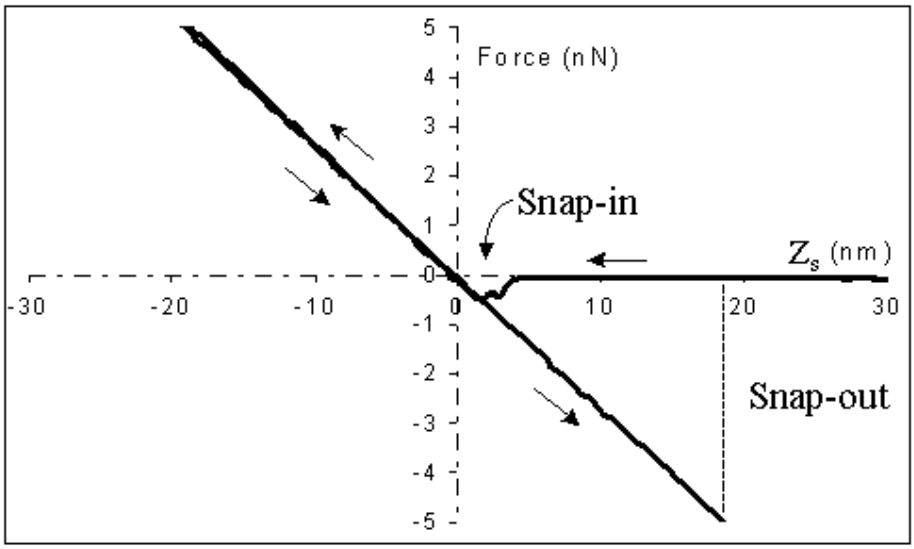

Figure 1.2: Typical force distance curves (one cycle of approach and retraction), acquired between a silicon nitride tip and a silicon wafer, in air. The force corresponding to the snap-out is always greater than the snap-in force due to sample deformations by the tip during the contact. Thus, the increased contact area increases the adhesion force. Moreover in ambient air, a water meniscus forms at the tip and acts against the tip pull- off from the surface.

1.2 Surface Forces

In 1986 G. Binnig et al. realized that they could easily make a cantilever with a spring constant weaker than the equivalent spring constant between atoms [26]. For example, the vibrational frequencies ω of atoms bound in a molecule or in a crystalline solid are typically 10^{13} Hz. Together with a mass m of the atoms in the order of 10^{-25} kg, a interatomic spring constants k (given by $\omega^2 m$) of about 10 N/m is received. For comparison, the spring constant of a piece of household aluminium foil that is 4 mm long and 1 mm wide is about 1 N/m. They recognized that by sensing Ångstrom-size displacements of such a soft cantilever spring, one could image atomic-scale topography. Furthermore, the applied force would not be large enough to push the atoms out of their atomic sites.

A force microscope measures the forces between two macroscopic bodies not between single atoms. This leads to several consequences. First, the net force is stronger than the intermolecular forces are and it acts at much larger distance. Even at 10-100 nm range, the interaction energy, which is proportional to the radius of the tip, can exceed k_BT (k_B is the Boltzmann constant, T the temperature). For example, when considering only the attractive force f in vacuum, it decays as $f \sim D^{-2}$ between a spherical tip and a flat surface (D being the tip-surface separation) compared to $f \sim r^{-7}$ for the attraction between two atoms (r being the distance between two atoms). The lower force gradient decreases the vertical resolution of the microscope. The long-range nature of the forces increases the effective interaction area and limits the lateral resolution. Secondly, the deformation of the bodies upon contact increases the contact area and results in additional contribution to the net force.

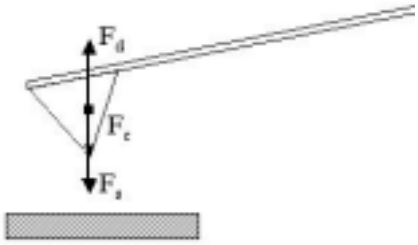

Figure1.3: Scheme of an AFM probe: a sharp tip mounted on a cantilever. The interaction force $F_i=F_s+F_d$ is a sum of many interatomic interactions, where F_s is the surface force and the force F_d results from the sample deformation. The interaction force is balanced by F_c due to the cantilever bending.

The forces that contribute to the net force exerted on the tip can be divided in three groups (Figure 1.3): (i) surface forces, F_s, (ii) forces due to the sample deformation, F_d, and (iii) the elastic force of the cantilever, F_c. All three forces can be of either sign.

(i) Surface forces. An elementary constituent of the interaction between a flat, rigid substrate and a sharp, rigid tip in vacuum is the pair potential between atoms at the tip and the sample. The origin of the intermolecular forces is essentially electrodynamic. At large distances (≈1-30 nm) the forces are attractive and are described by a van der Waals pair potential $w(r)=-C/r^6$, where C is the interaction constant determined by the polarizability and dipole moments of the molecules. Three different terms contribute to the van der Waals forces: the Keesom interaction (between two free rotating dipoles), the Debye interaction (between a dipole and a single charge) and London interaction (between induced dipoles). Usually the London or dispersion term is dominating. In order to relate the atomic interaction to the interaction between the macroscopic tip and the macroscopic substrate, one has to sum up all intermolecular potentials between each atom in the substrate and the tip [27]. For a sphere-surface potential, which is a good approximation for the interaction between the tip and the sample, the attractive part of the interaction energy becomes

$$W(D) = -\frac{AR}{6D} \tag{1.1}$$

where A is the Hamaker constant, R is the radius of the spherical tip, and D is the tip-surface distance (Figure1.4a). This gives the attractive force:

$$F_a = -\frac{dW}{dD} = -\frac{AR}{6D^2} \tag{1.2}$$

For a typical value of the Hamaker constant in vacuum, $A=10^{-19}$ J, the attractive force emerging between a tip with an apex radius of 10 nm and a surface separated by 1 nm distance is F_a=1 nN. This value sets an approximate scale of the forces that are sensed by the atomic force microscope.

The van der Waals force depends on the medium between tip and sample because the Hamaker constant contains the dielectric constants of all the three media (Figure 1.4b). In ethanol, for instance, the attractive van der Waals force is about 5 times smaller than in water. Therefore, imaging in ethanol does less harm to the sample because the interaction between tip and sample can be reduced. Van der Waals forces can even be repulsive if the two interacting solids are not made of the same materials and if the gap in between is filled with liquid of dielectric constant smaller or higher than the others two dielectric constants. In addition, the surrounding medium can contain ions and dissolved molecules. This can change the interaction potential in a complicated fashion, depending on the molecular composition, pH and ionic strength of the medium [27].

Under ambient conditions, the atmosphere contains water. Depending on the relative humidity, water can condense around the contact site and results in capillary forces (Figure 1.4c). The meniscus curvature varies with the relative vapour pressure and the tip shape [27]. For a spherical tip with radius *R*, when the shape of the meniscus is spherical and the radius of the meniscus is small compared to *R*, the capillary contribution to the adhesion force can be calculated as

$$F_{cap} = 4\pi R\gamma_l \cos\Theta \qquad (1.3)$$

where γ_l is the surface tension of the condensing vapour and Θ is the contact angle between the meniscus and the substrate. For water with γ_l=73 mN/m and small contact angle, the capillary force is F_{cap}=9 nN.

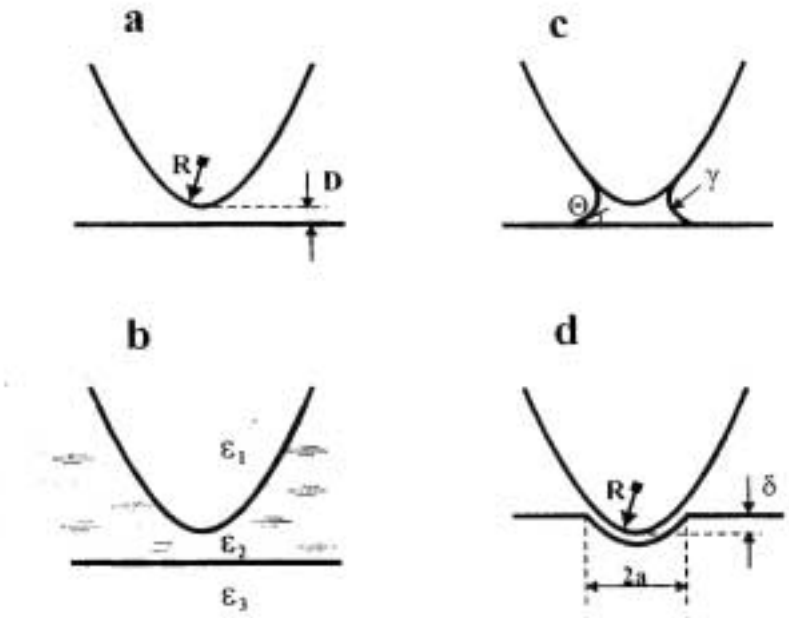

Figure 1.4: Different types of the tip-sample interaction: (a) rigid tip and rigid surface in vacuum, (b) interaction in a dielectric medium, (c) capillary condensation of water vapour in the contact area (d) deformation of a soft sample induced by a rigid tip.

At shorter distances (in the order of Å) the *repulsive forces* start to dominate. The repulsive interaction between two molecules can be described by the power-law potential $\sim 1/r^n$ (n>9) caused by overlapping of electron clouds resulting in a conflict with the Pauli exclusion principle. For a completely rigid tip and sample whose atoms interact $\sim 1/r^{12}$, the repulsion would be described by $W \sim 1/D^7$.

(ii) Forces due to the deformation of samples. So far the tip of the AFM and the sample have been assumed to be rigid. While this is often a good approximation for the tip, samples (especially organic specimen) are often significantly deformed elastically by the tip. The simplest approach to describe elastic deformation of the sample is the Hertz theory [27]. The relation between the deformation force F_d and the contact radius a is given by (Figure 1.4d):

$$F_d = \frac{Ka^3}{R} \tag{1.4}$$

where K is the elastic modulus of the tip-sample contact with $K = \frac{4}{3}\left[\frac{1-\nu_t^2}{E_t} + \frac{1-\nu_s^2}{E_s}\right]^{-1}$, E_t, ν_t and E_s, ν_s the Young's moduli and Poissons's ratios of the tip and sample, respectively. For a typical contact radius a=5 nm, K=l GPa and R=10 nm, the deformation force will be F_d=12.5 nN. In order to include the effect of the surface forces on contact deformation, two main models have been developed: Derjaguin, Muller and Toporov (DMT) and Johnson, Kendall, and Roberts model [27]. The choice of the model (DMT or JKR) depends on the experimental configuration in AFM force measurements. For large, soft solids, the JKR model describes the situation realistically. For small, hard solids it is appropriate to use the DMT model. In these model a "neck" is built between both solids in the contact area resulting in an enhanced contact radius (like a combination between Figure 1.4c and 1.4d). In the JKR model the contact radius a is given by the following expression:

$$a = \left(\frac{R}{K}\right)^{1/3}\left(F_d + 3\pi R w_a + \sqrt{6\pi R F_d w_a + (3\pi R w_a)^2}\right)^{1/3} \tag{1.5}$$

where F_d is the deformation force (or applied load), w_a is the work of adhesion. For w_a=0 the results of Hertz are obtained. The models have two consequences in common which are not included in the Hertz model. First, they predict a finite contact area even if no external force is applied and secondly, both require an opposite external force (pull-off or adhesion force) to separate the two bodies. For the DMT model the adhesion force is related to the surface energy γ (or to the cohesion energy $w_c=2\gamma$) of the solid surfaces in the medium used as

$$F_{adh} = 4\pi R\gamma \tag{1.6}$$

This equation assumes that the tip and the sample are of the same material. If the tip and the surface are made of different materials, the cohesion energy w_c should be replaced by the work of adhesion w_a. For a hydrocarbon polymer, where mainly dispersion forces are

responsible for the tip-surface interaction, the work of adhesion can be estimated as $w_a = 2\sqrt{\gamma_t^d \gamma_s}$, where γ^d_t denotes the dispersion part of the tip-surface energy of the tip and γ_s is the surface energy of the sample [27]. For a silicon tip and a hydrocarbon polymer surface (γ_t=100 mJ/m^2 and γ_s=25 mJ/m^2, respectively) the adhesion force will be about F_{adh}=6 nN.

The tip-sample deformation and the capillary forces are the two major factors that limit the lateral resolution of the sample because they increase the effective size of the probe.

(iii) Spring force of the cantilever. The interaction forces between sample and tip are balanced by the elastic force due to the cantilever bending: $F_c=k\Delta Z_c$, where k is the spring constant of the cantilever and ΔZ_c is the measured cantilever deflection. Summarizing, the deflection of the cantilever, ΔZ_c, results from a combination of deformation and surface force: $F_c=F_d+F_s$. For example, the total surface force between a polymer surface and an AFM tip can be estimated as $F_s\approx$15 nN [28]. With a cantilever of k=0.4N/m, a net repulsive force of 0.4 nN will be measured corresponding to 1 nm deflection. Since in this case the surface and deformation forces are of opposite sign (see Figure 1.3), they result of the same order of magnitude too. Therefore, surface forces should be as small as possible to minimise damage and indentation of soft polymer samples. For example, sharp probes show a lower capillary attraction and lower adhesion forces, and therefore enable gentler probing of a soft polymer than a blunt tip. A sharp tip can also be moved in and out of the sample layer more readily than a blunt tip. This is particularly important for tapping imaging mode described in the next Section.

1.3 Operating modes

AFM can be operated in many ways measuring different interactions between tip and sample and using different types of detection schemes. The two most utilised modes are: *Contact mode* and *tapping mode*.

Contact mode. When the AFM is used in contact mode (CM), it is operated in the so-called repulsive force regime between the tip and the sample. This means that during a scan, tip and sample are always in contact and the cantilever is bend away from the sample due to

the sample deformations. In this way one can achieve high spatial resolution (as high as 0.1 nm for the vertical resolution and 0.1 nm for the lateral resolution).

In contact mode, the surface structure can be imaged at *constant height* or at *constant force*. In the *constant height* mode the vertical distance between the base of the cantilever and the sample (Z_s) is kept fixed. The tip scans laterally across the sample (being x the scan direction) and from the change of the cantilever deflection one gets an image of the surface. The main drawback of this imaging mode is that, if the surface presents high steps, the tip is pushed against the step during the scan and it can be damaged. The more utilised mode is that at *constant force*. In this case the normal force between tip and sample, i.e. deflection Z_c, is maintained constant through a feedback loop.

In practice, at the beginning of an acquisition, the cantilever is approached to the sample until a certain value of the deflection, Z_{csp}, is measured. Then the tip moves laterally over another point on the surface and the deflection Z_c assumes a different value from Z_{csp}. At this point a feedback signal moves the sample vertically, approaching it to or withdrawing it from the tip, in order to reach the value Z_{csp} of the deflection. The *topography* or *height image* consists of the signals that the feedback sends to the piezoelectric translator in order to keep the deflection Z_{csp} constant. With a commercial AFM, a *deflection image* can be visualized simultaneously with the topography. A deflection image shows the difference between the measured cantilever deflection and the fixed value Z_{csp} (signal "C" in Figure 1.5). This difference is due to the fact that the control electronics of feedback loop does not respond instantaneously to changes on the specimen surface. When the sample surface presents slow variations in topography, the feedback has enough time to react and the deflection image is almost constant. When steep edges are present on the surface, the deflection image highlights them (Figure 1.6).

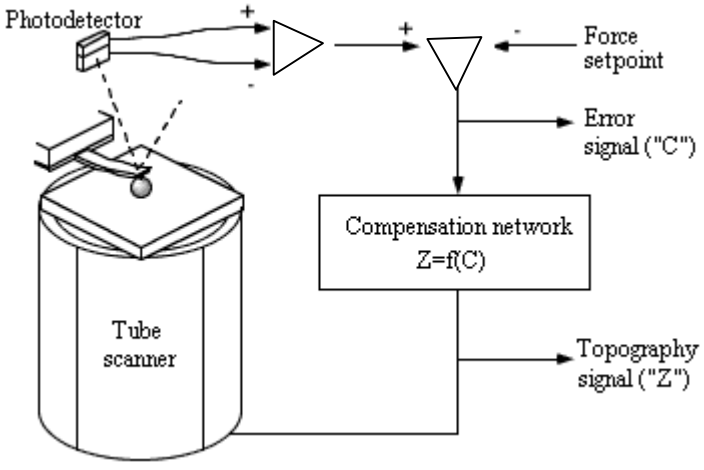

Figure 1.5: The AFM feedback loop. A compensation network monitors the cantilever deflection and keeps it constant by adjusting the height of the sample.

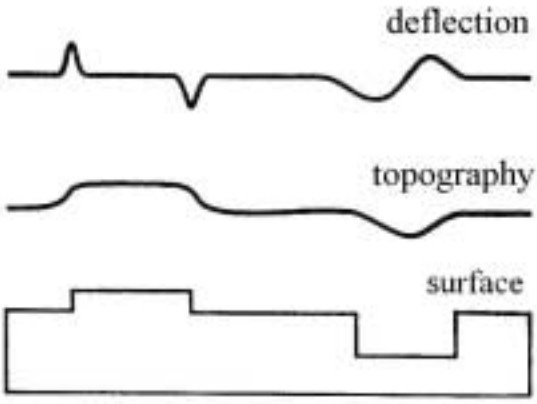

Figure 1.6: Example of a deflection and topography profile. The actual surface is shown below the profiles. The smearing out of the surface features in the topography profile is due to the tip shape and dimension (see Sect. 1.4)

Tapping mode. A severe drawback of the contact mode is that the native structure of soft samples can be easily distorted due to deformation forces that are originated from the tip-sample contact, and shear forces that are attributed to the lateral scan movement. In *tapping mode* both forces are minimized. This is realized by oscillating the cantilever with a piezoelectric element near its free resonant frequency ω_0 (≈300 kHz) [29]. The tip rapidly moves in and out of the sample surface so that it stays in contact only for a short time interval of the oscillation period. Due to the short interaction time, tapping mode allows high resolution imaging on viscoelastic materials, like polymers or biological samples [30,31]. Because of the viscoelastic properties, the sample behaves as "rigid" material during the short interaction time and became less susceptible to deformation. The amplitude ranges from 5 to 100 nm. It is sufficiently high to overcome adhesion forces due to capillary condensation when imaging in air.

In *tapping mode* the change of the oscillation amplitude due to the tapping of the tip against the surface is measured. Figure 1.7 outlines the variation of the tip deflection as the oscillating cantilever is moving towards the surface [32].

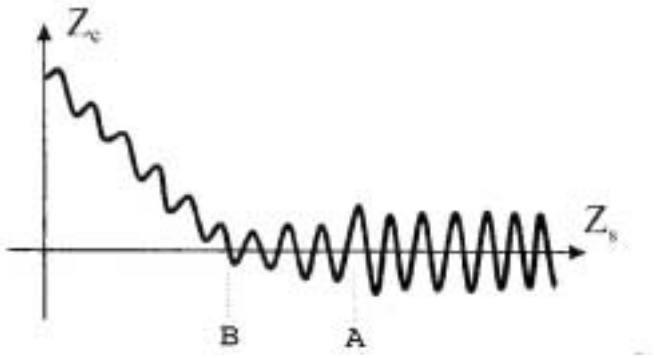

Figure 1.7: Variation of the cantilever deflection Z_c as the oscillating cantilever approaches the sample surface. Z_s is the distance between the cantilever base and the surface.

When the cantilever moves towards the sample with constant vibration excitation near the free resonant frequency, three regimes can be distinguished. At large distances, the cantilever oscillates with constant amplitude that is determined by viscous damping of the cantilever in air. At a certain separation ('A' in Figure 1.7) the tip begins to tap against the sample, limiting the amplitude (second regime). The amplitude then reduces approximately linearly with decreasing separation (suggesting that the amplitude is limited by the distance between the cantilever equilibrium position and the sample surface). As the cantilever is moving closer to the sample ('B' in Figure 1.7), at a certain separation the amplitude of the cantilever drops abruptly (third regime). At this point the cantilever has no longer sufficient energy to break away from the surface adhesion and the tip gets stuck to the sample. Now the amplitude stays approximately constant but the mean deflection changes by the same amount of the sample movement as occurs in the contact region in contact mode (see figure 1.2). During an image the AFM is operated in the first regime. The deviation of the amplitude signal from a certain set-point value A_s is used by a feedback loop to maintain the separation between the tip and sample constant, and hereby visualize the surface structure. In tapping mode it is possible to visualise *topography* and *amplitude* image that corresponds to the topography and the deflection image of the contact mode. When the surface composition is uniform, the amplitude variation is mainly caused by the surface topography. However, if the surface is heterogeneous, the variation in the amplitude can be affected by local differences in composition, in viscoelasticity [33-35], adhesion [36] and friction of the sample. These variations can be detected by measuring the phase difference between the oscillations of the cantilever driving piezoelectric translator and the detected oscillations (*phase* image). The direction of the curve shift of both, the amplitude and the phase curve depends on the tip-sample interaction. For a freely

oscillating cantilever characterised by the spring constant *k*, effective mass *m* (that consider the mass of the tip and a distribution mass for the cantilever), quality factor *Q*, and resonance frequency ω_0, the phase angle φ of the free cantilever oscillation (in radians) is expressed as a function of the vibration frequency ω

$$\varphi = \tan^{-1}\left(\frac{m\omega\omega_0}{Q\left(k - m\omega^2\right)}\right) \tag{1.5}$$

At $\omega = \omega_0$, φ is $\pi/2$. To a first approximation, the essential consequence of the tip-sample interactions is to change the spring constant of the cantilever to a new effective value $k_{eff} = k + \sigma$, where σ represents the sum of the force derivatives for all the forces F_i acting on the cantilever[35]

$$\sigma = \sum_i \frac{\partial F_i}{\partial Z_s} \tag{1.6}$$

Z_s represents the distance between the cantilever base and the surface. The phase angle φ (in units of radians) of the interacting cantilever can be expressed as

$$\varphi = \tan^{-1}\left(\frac{m\omega\omega_0}{Q\left(k + \sigma - m\omega^2\right)}\right) \tag{1.7}$$

provided that $\sigma << k$. Then the phase angle φ_0 (i.e. φ at ω_0) is given by

$$\varphi_0 = \tan^{-1}\left(\frac{k}{Q\sigma}\right) \tag{1.8}$$

The phase shift, $\Delta\varphi_0$, between the free and the interacting cantilever at $\omega = \omega_0$ is:

$$\Delta\varphi_0 = \frac{\pi}{2} - \tan^{-1}\left(\frac{k}{Q\sigma}\right) \approx \frac{Q\sigma}{k} \tag{1.9}$$

The sign of the phase shift $\Delta\varphi_0$ coincides with that of the overall force derivative σ. Thus, the phase shift is positive when the overall force acting on the tip is attractive, and negative when the over all force is repulsive. Compared to the amplitude, the phase is more sensitive to the sign of the forces and to the tip-surface distance.

Concluding, the main advantages of the tapping mode over conventional contact AFM are:

- Normal forces exerted on the sample can be minimised due to the enhanced sensitivity towards small variations in amplitude at the resonant conditions. Thus, the tapping mode becomes applicable for imaging *soft* and fragile samples.

- There are no lateral forces that can damage the sample or the tip because the tip only contacts the surface briefly during each oscillation. This property is of primary importance for imaging of objects that do not adhere strongly to the substrates.
- Finally, the cantilever oscillates at high frequencies from 50 to 500 kHz, where many viscoelastic materials, such as polymers, respond elastically.

Most of the measurements shown in this work have been done in tapping mode.

1.4 Imaging with the AFM

The resolution in AFM depends on the effective size of the probe. For the visualisation of features on a sample, the size and the shape of the tip become important since the tip shape and the surface topography may superimpose. For small tips imaging large but flat objects the interpretation of an image is relatively simple: The tip behaves as a point like probe and the measured topography is authentic. Unfortunately, this often is not the case and the image is determined by the geometry of both. This is shown in Figure 1.8 where a periodically corrugated sample is scanned by a tip with a spherical end. When the tip size becomes comparable to the wavelength of the surface corrugation, depressions appear smaller while protrusions appear flatter. The lateral distance between the protrusions is not affected by the shape of the tip. Even if the tip shape is known, the true surface cannot totally be reconstructed by image processing because the resulting images contain no information about the structure of deep dumps. Moreover, the effective size of the tip is modified from tip-sample interactions. For example, the effective size increases because of elastic or inelastic deformation of the sample (if an object is highly deformable the resolution decreases). Also, surface roughness and capillary forces contribute to increase the effective size of the probe.

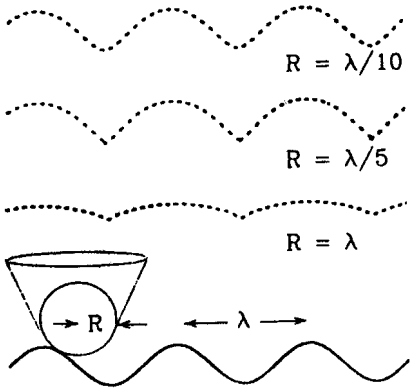

Figure 1.8: Possible profile of a corrugated surface according to the tip radius.

The smoothness of the substrate can also influence the resolution. In many applications it is difficult to distinguish the object from the substrate, for example when the substrate is

too rough compared to the adsorbate dimension. The smoother the substrate the better the resolution of objects deposited onto the substrate.

Experimentally, the resolution is limited by the sensitivity of the force detection system, the electronic noise, and the scanner precision.

Regarding the visualisation of atomic structures with an AFM, one needs to distinguish between the resolution of periodic structures and of single objects.

Despite the relatively large contact radius in contact mode AFM (from 1 to 20 nm), atomic lattice images were obtained on organic and inorganic substrates [37] (Figure 1.9). However, atomic defects or single atoms adsorbed to a substrate were rarely imaged. In other words, with an AFM the visualisation of the crystalline lattice is achievable while a true atomic resolution is exceptional. The visualization of crystalline lattices was explained with the Moiré mechanism that can occurs when two lattices slide one over the other and generate periodic fringes within the interaction region [38]. Thus, the AFM gives a lattice image similar to diffraction techniques. To approach the true atomic resolution, the aperture of the tip must be decreased as far as possible by using sharper tips and operating at low forces to minimize the contact area. Any distortion of the sample, in particular inelastic deformation, can disturb lattice imaging and makes visualisation of lattice defects impossible. Operation in liquid results in smaller sample deformation and might prevent the destruction of tiny asperities at the tip end [39]. By minimizing the adhesion force Binnig et al. has observed different types of point-like defects on the (1014) cleavage surface of calcite [40]. In contradiction to this approach, Magonov et al. demonstrated well-resolved atomic-scale images of inorganic layered crystals with defects which were scanned with high repulsive forces up to several hundred nanoNewton [41]. It has been suggested that in this case under the strong repulsion condition, a few outermost atoms might dominate the force facilitating the detection of point-like defects.

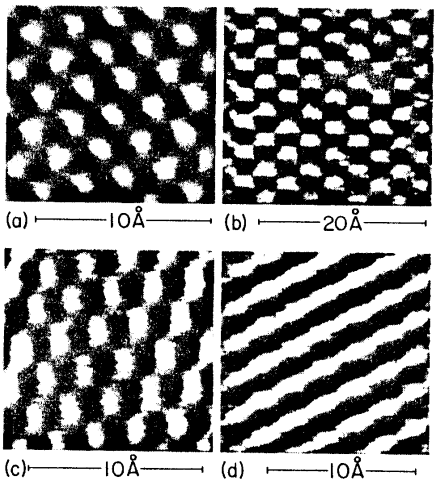

Figure 1.9: First images of atomic resolution of a periodic sample obtained by Albrecht and Quate[37]. (a) HOPG (b) molybdenum disulfide, (c) boron nitride, (d) also boron nitride but with less defined tip. Images were taken in contact mode.

1.5 Dendrimers

Dendrimers (greek: dendron=tree, meros=part) are a class of molecules with a well-defined tree-like architecture. They emanate from a core and like a tree they more and more ramify with each subsequent branching unit. After the publication of the first papers [42-44], which dealt with the development and the realization of this new molecular architecture but which were limited by the little developed analytical methods, the interest on this research field increased rapidly in the past two decades [45]. The dendrimer synthesis consists of steps, each of which is called generation, to build up the molecule. There are two fundamental synthesis concepts [46]:

1) The *divergent* method in which the synthesis is started from a multifunctional core molecule and one branching unit after another is successively attached to the core molecule (Figure 1.10). This way the dendrimer can be built up step by step until steric effects prevent further reactions of the end groups.
2) The *convergent* method in which the synthesis is started at the periphery and elaborated to the core (Figure 1.11). The skeleton is constructed stepwise starting from the end groups towards the inside and is finally covalently attached to a core molecule to yield the dendrimer.

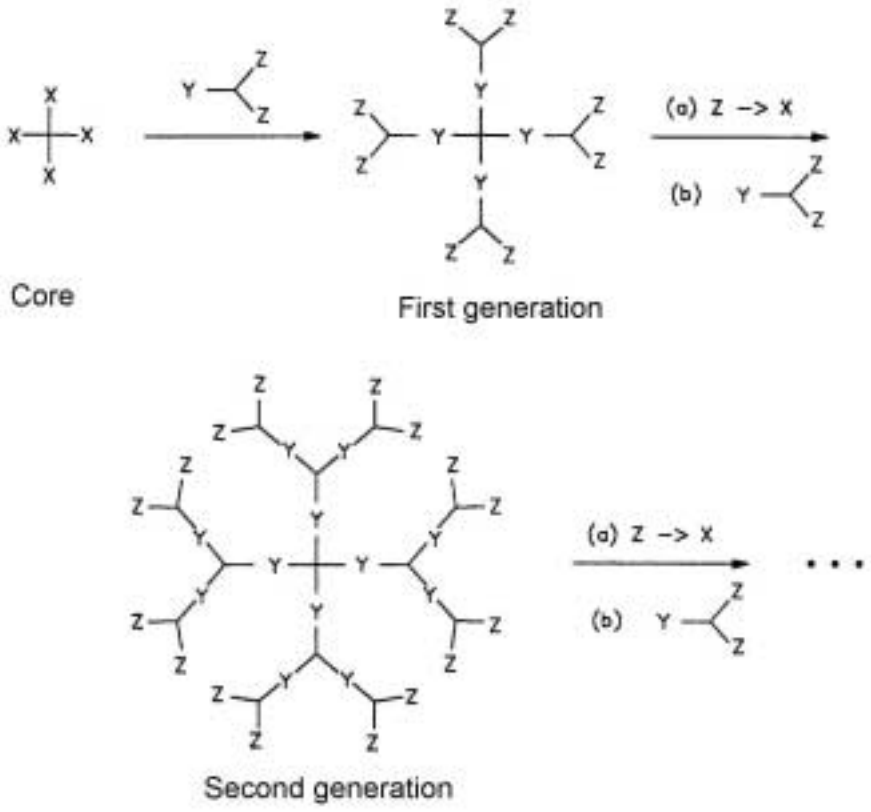

Figure 1.10: Sketch of the divergent method for the synthesis of a dendrimer.

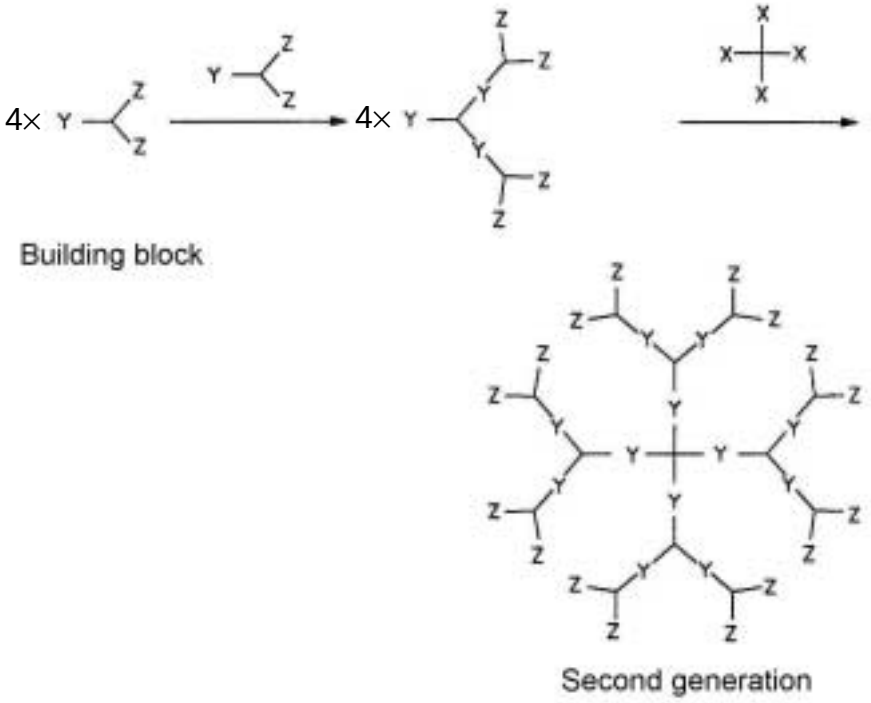

Figure 1.11: Sketch of the convergent method for the synthesis of a second generation dendrimer.

In the divergent synthesis of dendrimers structural defects might accumulate with the built-up of further generation, leading to an incomplete reaction at the end groups. Here a chromatographic separation of the by-products sometimes is impossible because they reveal similar physical properties. In the convergent synthesis, in contrast, a segment growing with each reaction step is coupled with only one branching unit. Thus, this approach facilitates the removal of undesired by-products, for example, by means of gel permeation chromatography (GPC), though it does not allow the formation of as many generations as the divergent method because of steric problems that arise from the reaction of the segments and the core molecule.

Higher generation dendrimers reach high molecular masses (some thousand and higher, compared to polymers) and are characterized by a narrow distribution of the molecular masses (monodispersity), compared to macromolecules obtained through polymerisation reactions. Dendrimers have a well-defined shape, determined by a covalently skeleton, and functional groups in the outer shell. Thus, they may be compared to natural globular biomacromolecules, the shape of which is , in contrast, determined hydrogen bonds.

One of the first works on the three-dimensional structure of divergently synthetisised dendrimers was published by de Gennes and Hervert [47]. They concluded from a mathematical growth model that the lower generation dendrimers, should be rather flat,

with ellipsoidal shape and each branch is directed radially towards the outside, with the ends groups lying on the surface of an ellipsoid. Later generations transform the macromolecules into a more spherical shape from a certain generation upwards (depending on the core molecule, branching multiplicity, and the length of the branch segment). The model indicates that the dendrimers can grow up until a critical branched state is reached and prevents further reaction for steric hindrance between the external groups. Hence, the molecules are thought to be spherical constructions with a dense exterior and a loose interior with channels and cavities. Actually, the localization of the end groups in dendritic systems depends critically on the structure of the dendrimer in question [48]. Most of the known dendrimers are flexible with the end groups throughout the dendrimer volume. However, when the end groups can communicate with each other via secondary interactions such as π-π interactions, electrostatic repulsion, hydrogen-bonding interactions or hydrophobic effects, the dendritic terminal units will assemble more efficiently at the periphery, thereby precluding backfolding.

The high density of external functional groups gives the possibility of multiplying certain functionalities. For example, dendrimers have been utilised in medicine as agents in diagnostic or in therapeutic treatments. They have been tested as a contrast agent for magnetic resonance imaging (MRI) to visualize the bloodstream in the body [49]. The molecule consists of a trimesinic acid central building block, to which second-generation lysine dendrons with a total of 24 complexed gadolinium ions are anchored. These dendrimers have revealed several advantages on other clinically used contrast media e.g. a quantitative renal elimination and a high intravascular retention time (thanks to the high molecular weight) that allows a well resolved and contrasted visualization of the blood vessels. Dendrimers have been applied in boron neutron capture therapy as well. This therapy represents a method for the treatment of presently incurable forms of cancer. The high neutron capture cross-section of the ^{10}B isotope for thermal neutrons is used to produce a radiation energy that is lethal for the surrounding cells. The aim is to realize a compound as boron-rich as possible which can be selectively coupled to molecules that recognize tumour cells. Moroder et al. developed the first lysine dendrimers that specifically coupled to proteins and carries 80 terminal boron atoms on the end groups [50].

The peculiarities of dendritic structures offer new possibilities to manipulate the properties of solid surfaces by coating them with dendrimers. As result of their catalytic [21], binding [22], and optical [23] properties, supramolecular assemblies of dendrimers have potential

applications as chemical sensors [24] and photosensitive materials [25]. A change in conformation, compared to that in solution, has been noticed on dendrimers layers formed at the interfaces, either gas-water or gas-solid. The extent of the conformational changes depends on the strength of the interaction between the molecules and the substrate and between the molecules [51,52]. The stronger the attractive forces, the more flattened the spherical shape becomes and the more it resembles a disc. As reflected in the "phase diagram" (Figure 1.12), the mode of adsorption of the dendrimers is dependent on the adsorption strength and on the generation number (higher generation dendrimers have more interaction sites per molecule and therefore, these dendrimers have a better chance to be strongly adsorbed).

The anisometric changes of the molecular shape can be prevented by reducing the adhesion forces and increasing the branching density [53]. For dendrimers with a high branching density, they might keep their spherical shape. Moreover, the high branching density prevents overlapping and cause molecular segregation. The well defined geometry and the low polidispersity of such molecules favours preparation of nanoscopically ordered films.

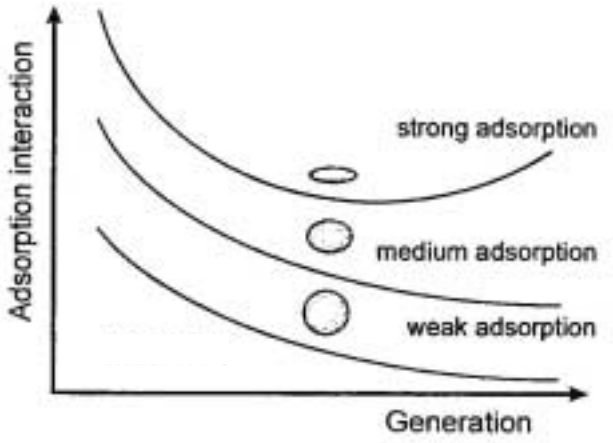

Figure 1.12: A „phase diagram" that shows how the shape of dendrimers on adsorbed monolayers depends on the strength of the adsorption interaction and the dendrimer generation. The data are based on Monte Carlo simulations by Mansfield [50].

Dendrimer construction can be combined with polymer synthesis to obtain polymers with rigid cylindrical shape from flattened spherical ones [54]. Schlüter et al. describe the class of dendronized polymers that are comb-like polymers with a backbone of conventional polymers like polyacrylate or polystyrene and with the comb's teeth being dendrons (dendrimer branches) (Figure 1.13). Depending on the dendrons structure, size, and grafting density along the backbone, the polymer backbones can attain different conformations from random coils to fully stretched linear molecules. This stiffening of the

backbone is caused by the steric repulsion between the pendant dendrons and finally provides cylindrical objects that can be rigid on a longer scale than individual chains. On a surface they form large, ordered, two-dimensional arrays in which the individual rods are packed parallel to each other. Such parallel arranged, nanometer-scale objects on surfaces are interesting for a number of applications, for example as polarizers, polarized emitters, or orienting elements in liquid crystals displays.

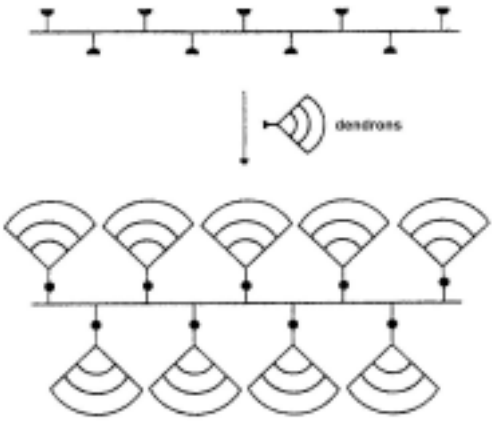

Figure 1.13: Scheme of dendrons anchoring to a polymeric backbone.

Because of the small size of dendrimers, it is rather difficult to achieve molecular resolution and visualize single molecules by conventional techniques. Recently, cryo-TEM has been used to image individual molecules of poly(amidoamine) from generation 5 to generation 10 [55]. The AFM is a powerful tool to observe the topography of absorbed polymers on surfaces. Using AFM, dendritic structures have been studied on a variety of surfaces, such as mica [13], graphite [56], glass [57], and silicon surface [58]. Usually, it shows some grainy or corrugated surface structure on a solid substrate, where the grain size was much greater than the molecular diameter. This was ascribed to deformed molecules compared to the non adsorbed ones [58,59]. Layers with isolated dendrimer molecules could be prepared by adsorption from dilute solutions using short exposure time [60]. The polydispersity is characterised by statistically measuring the dimension of the adsorbed molecules. A narrow size distribution from 100 to 400 nm in diameter for highly branched molecules has been found by AFM in agreement with light scattering and TEM measurements [60].

2 Materials and Methods

2.1 Synthesis of the dendrimers

The alkyl substituted polyphenylene dendrimers utilized in the present thesis were synthetised in the group of Prof. Müllen from the Max Planck Institut für Polymerforschung, Mainz, Germany. These dendrimers consist of an inner part of twisted, interlocked phenyl rings and an external shell of alkyl chains [61,62]. The presence of polyphenylene rings in the inner part should make the molecule stiff as the rotation is only possible around the inter-ring C-C bonds. Furthermore, polyphenylenes posses a high chemical and thermal stability [63]. The combination of a persistent structure, properties like thermal stability, processability, variability and surface functionalization make them promising tools, e.g. as intermediates for drug-carriers.

The nomenclature that I am going to utilise in the following chapters is described in Figure 2.1. The utilized dendrimers were different for the core molecules and for the external functional groups. The index numbers for the position of the external chains refer to the number of the benzene ring in which substitution occurs. They were second generation dendrimers synthetized in the divergent method. The key step in the dendrimer synthesis is the repeated [4+2]-cycloaddition of a building block like **3** (see Figure 2.2 and Figure 2.3) to an ethynyl-substituted core and subsequent deprotection [62]. In the case of dendrimers $Td_{2,3}$-$(C_{12}H_{25})_{16}$ and $Td_{1,4}$-$(C_{12}H_{25})_{16}$, starting point of the synthesis is the tetrahedric core tetra-(4-ethynylphenyl)-methane (**1**) (Figure 2.2) [64], whereas in the case of dendrimer $Tri_{2,3}$-$(C_{12}H_{25})_{16}$ 1,3,5-triethynylbenzene (**2**) [65] is used as core (Figure 2.3). By Diels-Alder [4+2]-cycloaddition of the cores with 3,4-bis-(4-triisopropylsilylethynylphenyl)-2,5-diphenylcyclopentadienone (**3**) in refuxing *o*-xylene the triisopropylsilylethynylated first generation polyphenylene dendrimers **4** (Figure 2.2) and **10** (Figure 2.3) can be synthesized in quantitative yields. Deprotection of these dendrimers with tetrabutylammonium fluoride in THF gives the ethynylsubstituted dendrimers **5** (Figure 2.2) and **11** (Figure 2.3) also in quantitative yields.

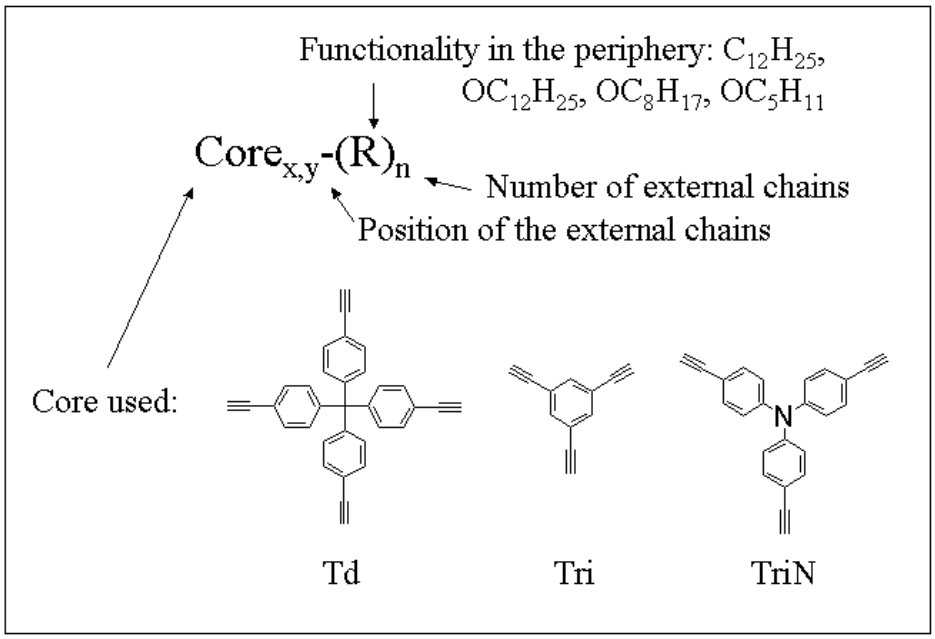

Figure 2.1: Nomenclature of polyphenylene dendrimers.

The alkylated dendrimers $Td_{2,3}$-$(C_{12}H_{25})_{16}$ and $Td_{1,4}$-$(C_{12}H_{25})_{16}$ (**8** and **9** in Figure 2.2) are synthesized by Diels-Alder [4+2]-cycloaddition of **5** with the dodecyl alkylated tetraphenylcyclopentadienones **6** and **7**. Dendrimer $Tri_{2,3}$-$(C_{12}H_{25})_{16}$ is obtained by the cycloaddition of **11** (Figure 2.3). In the case of $TriN_{2,3}$-$(C_{12}H_{25})_{16}$ dendrimer, the starting point of the synthesis is the core tri-(4-ethynylphenyl)-amine (Figure2.1); the rest of the synthesis is the same as for $Tri_{2,3}$-$(C_{12}H_{25})_{16}$ dendrimer (Figure 2.3). The synthesis of $Td_{2,3}(OC_xH_{2x+1})$ (where x=12, 8, 5) dendrimers is the same like for $Td_{2,3}$-$(C_{12}H_{25})_{16}$ until the first generation (Figure 2.2). To introduce alkoxy chains on the periphery, 3,4-Bis-(4-methoxy-phenyl)-2,5-diphenyl-cyclopentadienone (like molecule **6** in Figure 2.2 with methoxy groups in the position of R1 instead of the dodecyl chains) was used in the Diels–Alder cycloaddition forming the second generation of the dendrimer. After treatment with Borontribomide, terminations of the external molecules are hydroxy groups. The final molecule is obtained via coupling reaction with the corresponding n-bromoalkane.

After isolation by column chromatography, the dendrimers are obtained as white powders, with good solubility in solvents like THF, chloroform, toluene, or hexane and thermal stability to temperatures higher than 300°C. The purity and monodispersity of each step of the synthesis and of the final products was checked with NMR (Nuclear Magnetic Resonance) and MALDI-TOF MS (Matrix Assisted Laser Desorption/Ionisation-Time of Flight Mass Spectrometry). The values of the molecular masses are listed on Table 2.1.

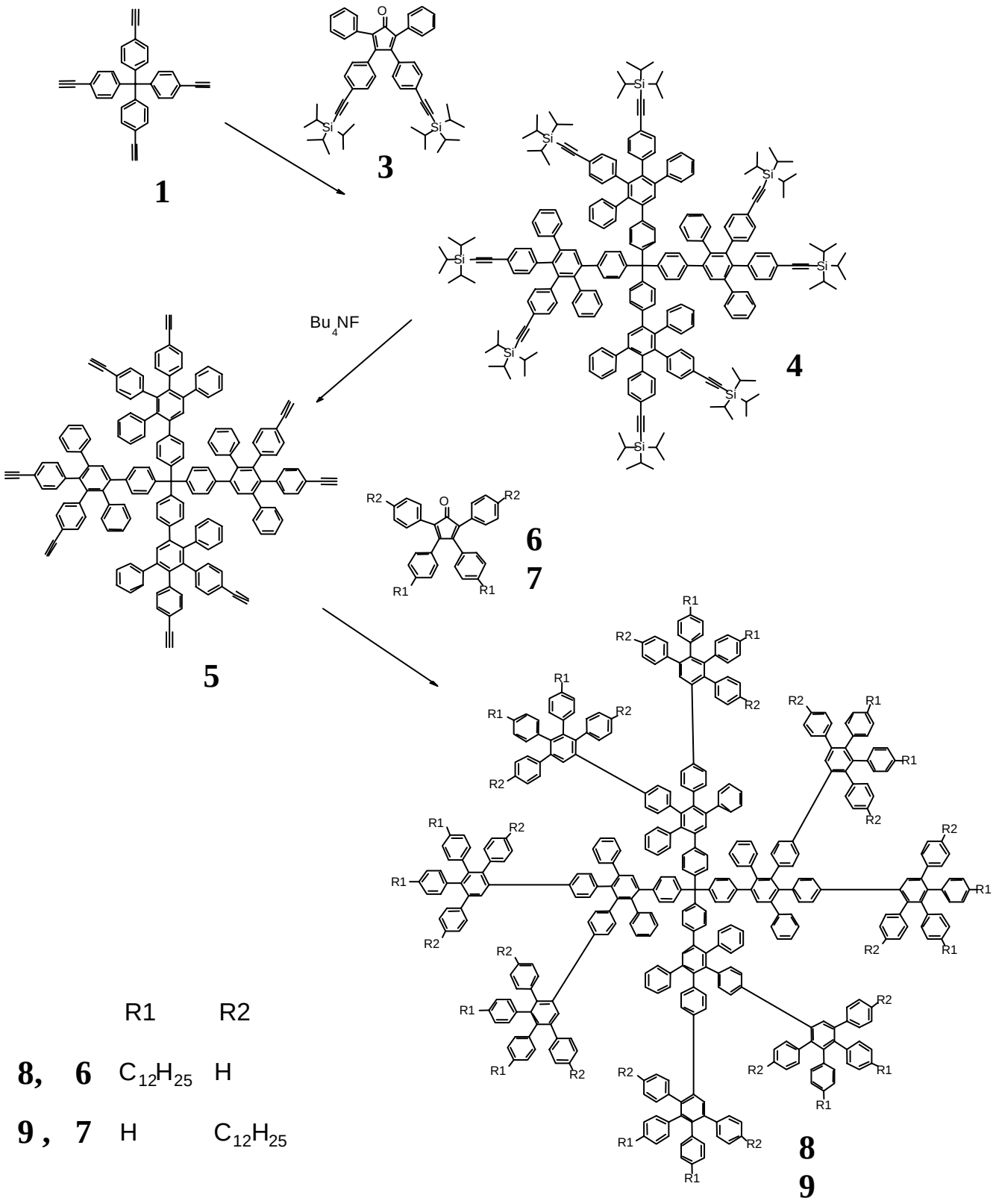

Figure 2.2: Synthetic pathway for $Td_{2,3}$-$(C_{12}H_{25})_{16}$ and $Td_{1,4}$-$(C_{12}H_{25})_{16}$ dendrimers (8 and 9 in the figure).

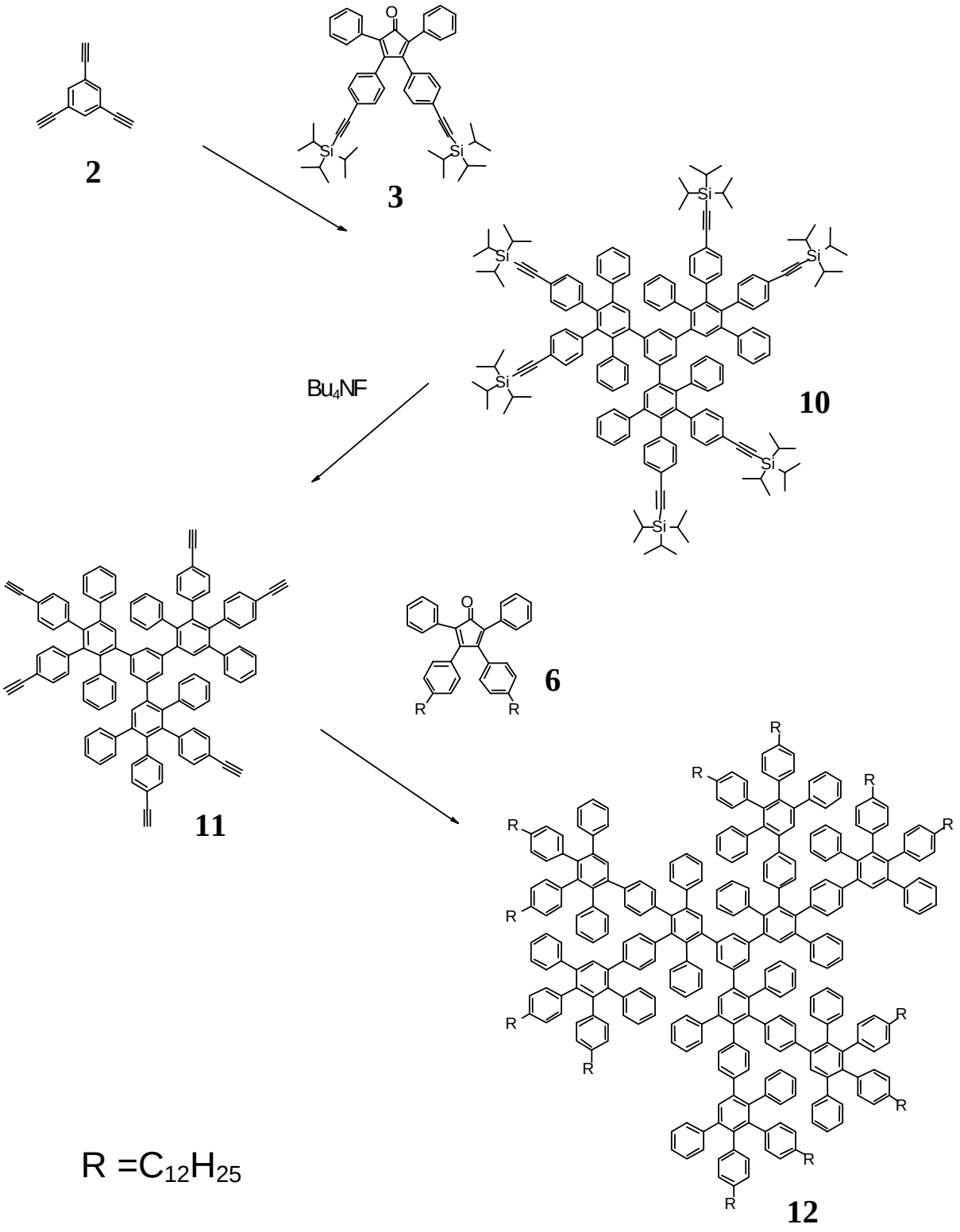

Figure 2.3: Synthetic pathway for $Tri_{2,3}$-$(C_{12}H_{25})_{16}$ dendrimer (12 in the figure).

Space Filling Models of the Corresponding Second Generation Dendrimers

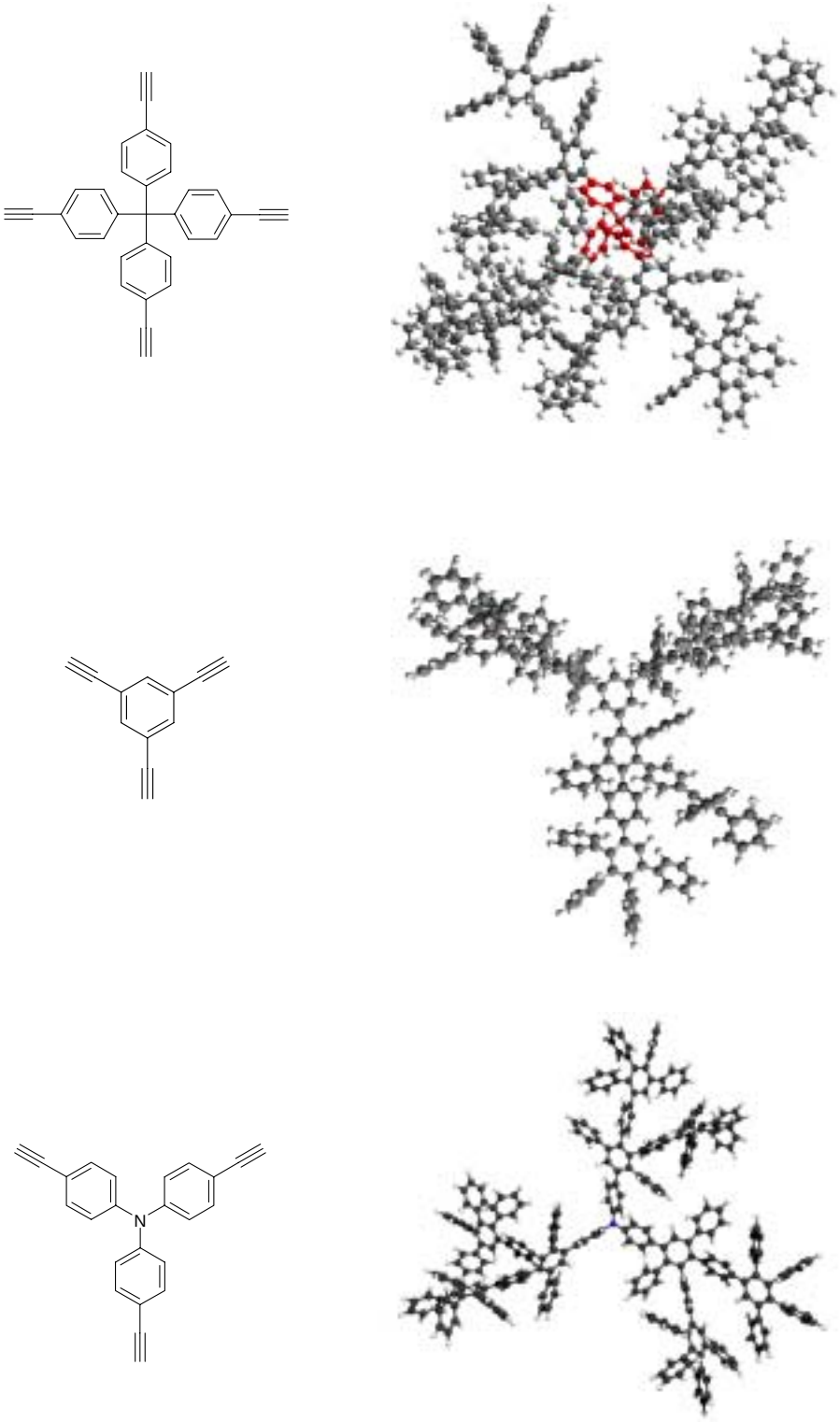

Figure 2.4: Core molecules and corresponding second generation dendrimers. The space filling representations are calculated with Cerius^2 molecular simulation software.

Dendrimer	Molecular mass (g/mol)	Diameter (nm)
$Td_{2,3}$-$(C_{12}H_{25})_{16}$	7579	4.5
$Td_{1,4}$-$(C_{12}H_{25})_{16}$	7579	4.5
$Tri_{2,3}$-$(C_{12}H_{25})_{12}$	5522	3.9
$TriN_{2,3}$-$(C_{12}H_{25})_{16}$	5690	4.4
$Td_{2,3}$-$(OC_{12}H_{25})_{16}$	7892	4.5
$Td_{2,3}$-$(OC_8H_{17})_{16}$	6938	4.5
$Td_{2,3}$-$(OC_5H_{11})_{16}$	6265	4.5

Table 2.1: List of the molecular masses and of the core diameter (without external chains) from the molecular simulation.

A first impression about the shape and the size of dendrimers is obtained by molecular mechanic simulations [66,67] (Figure 2.4). Dendrimers $Td_{2,3}$-$(C_{12}H_{25})_{16}$, $Td_{1,4}$-$(C_{12}H_{25})_{16}$ and $Td_{2,3}$-$(OC_xH_{2x+1})_{16}$ have an overall tetrahedral shape due to the central carbon atom. The simulated diameters of the polyphenylene dendrimers (without alkyl chains) are 4.5 nm. The $Tri_{2,3}$-$(C_{12}H_{25})_{12}$ dendrimer has a propeller-like shape with a diameter of the polyphenylene dendrimers (without alkyl chains) of 3.9 nm. In $TriN_{2,3}$-$(C_{12}H_{25})_{12}$ the central phenylene unit is replaced by a triphenylamin unit. As a consequence the overall shape is changed from a flat propeller to tetrahedral with one missing arm. The diameter of the polyphenylene molecule is 4.4 nm. The diameters of the molecule were confirmed by light scattering and TEM measurements [62].

2.2 Sample preparation

Before coating the substrates, dendrimers were dissolved in dichloromethane or dichlorobenzene p.a. (Merck, Darmstadt, Germany) at a concentration between 1 µg/ml and 0.2 mg/ml. The substrate utilised were HOPG (highly oriented pyrolytic graphite) and muscovite mica, purchased by Plano GmbH, Wetzlar, Germany. These substrates are suitable for AFM measurements since they can easily be cleaved with adhesive tape, and one obtains atomically flat surfaces on area larger than several cm.

Dendrimers layers have been prepared by spin coating. A drop of the solution is deposited on the freshly cleaved surface and the sample is rotated at a constant speed until the solvent evaporates. Spin coating is a standard coating method for obtaining thin (1 nm-1 μm), uniform, and homogenous films on solid surfaces, widely used in some technical fields such as microelectronics. The mechanism of film formation was described by Weill in 1986 [68]. He considered two simultaneous transport phenomena: the radial flow of the solution along the *r* axis (parallel to the surface) and the evaporation of the solvent perpendicular to the surface (*z* axis). Due to the radial flow the height of the solution decreases with time (Figure 2.5, a and b). Due to the evaporation of the solvent perpendicular to the surface a concentration gradient along the *z* axis is created. The concentration of polymers, *C*, increases from the substrate to the top of the layer. When the concentration at the top of the layer reaches a critical value, for which the solution behaves like an elastic solid, the layer becomes phase separated (Figure 2.5, c). Two phases coexist: a bottom viscous layer, whose thickness decreases continuously with time, and an upper elastic "crust", made of polymer gel, whose thickness increases with time (Figure 2.5, d). The radial flow stops after the all viscous phase is disappeared. At that time the mass of the polymer on the substrate is constant and the layer is only subject to solvent evaporation which further decreases its height.

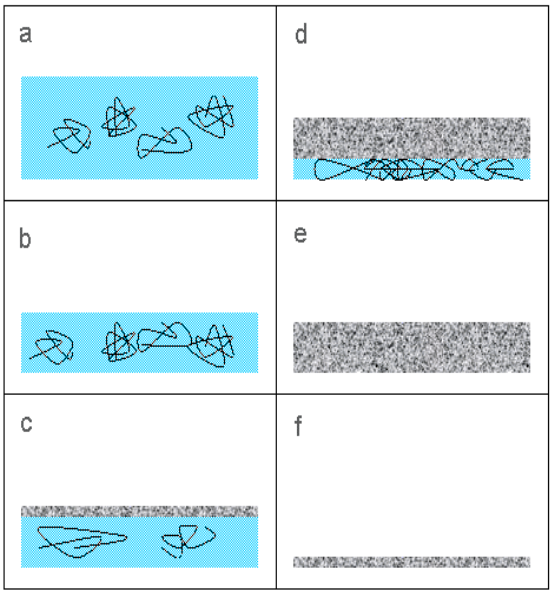

Figure 2.5: Schematic representation of the film formation during spin coating.

There are a number of empirical investigations on the formation of spin-coating films [69,70]. The final thickness of the film depends both on the system solute/solvent/substrate and on the application parameters, like the rotating speed, the rotating time and the time interval between putting the solution on the substrate and the onset of the rotation. As expected, we found that increasing the concentration of the polymer solution the thickness increases (see Sect. 3.1.1). For a given polymer solution, the thickness of the film decreases with increasing rotating speed. It increases when one waits some time between putting the drop of solution on the substrate and the onset of the rotation.

Our samples have been prepared depositing 50 µl of the dendrimer solution on the substrate and immediately rotating at 810 r.p.m. for 10 s on a home-built spin-coater.

2.3 Atomic Force Microscope

Samples were imaged at room temperature with a commercial AFM (Nanoscope III) from Digital Instruments (DI), Santa Barbara, California. For tapping mode we used rectangular silicon cantilevers (Nanosensors, Wetzlar, Germany), 125 µm long, 30 µm wide, 4 µm thick, with an integrated pyramidal tip, with a nominal spring constant of 42 N/m, and a resonance frequency of 330 kHz. Contact imaging was done with V-shaped silicon nitride cantilevers (Digital Instruments, 110 µm long, 40 µm width, 0.6 µm thick, spring constant roughly 0.11 N/m). A piezoelectric scanner type E (DI) was utilized; it allows a maximum x,y-scan of 10 µm and a z extension of 2.5 µm. The scanner was calibrated in the x,y-plane by imaging a rectangular grid of 1 µm mesh size (DI) and in z-direction with an interferometric method as described in ref. [71]. The control of the microscope, the data recording and the image process were realised with the Nanoscope-Software provided by DI.

The instrument scans over a squared section of the sample surface. With the DI software it was possible to choose the centre of the scanned area, the lateral dimension and the scan direction relative to the sample. The most consistent images were received for 10 min in tapping mode and about 2 min in contact mode. The raw data were modified with the software in order to have every scan line at the same average height (Flatten). For repeated structure on the sample, the “Spectrum 2D” (two-dimension) function allowed to transform images into a 2D Fast Fourier transform plot (2DFFT). The height of the adsorbed layers was determined in two ways. First, from cross sections of images which include a hole in the layer (Figure 2.6, top). Second, from cross sections of areas which include a region that has been scraped free before (Figure 2.6, bottom). In this way we could know that we observed a monolayer and not multiple layers, one placed on the top of the other. To scrape the graphite free an area was scanned roughly 5 times in contact mode at a force of 100-200 nN (scanning with forces significantly higher than 200 nN destroyed the graphite structure and much deeper holes were formed).

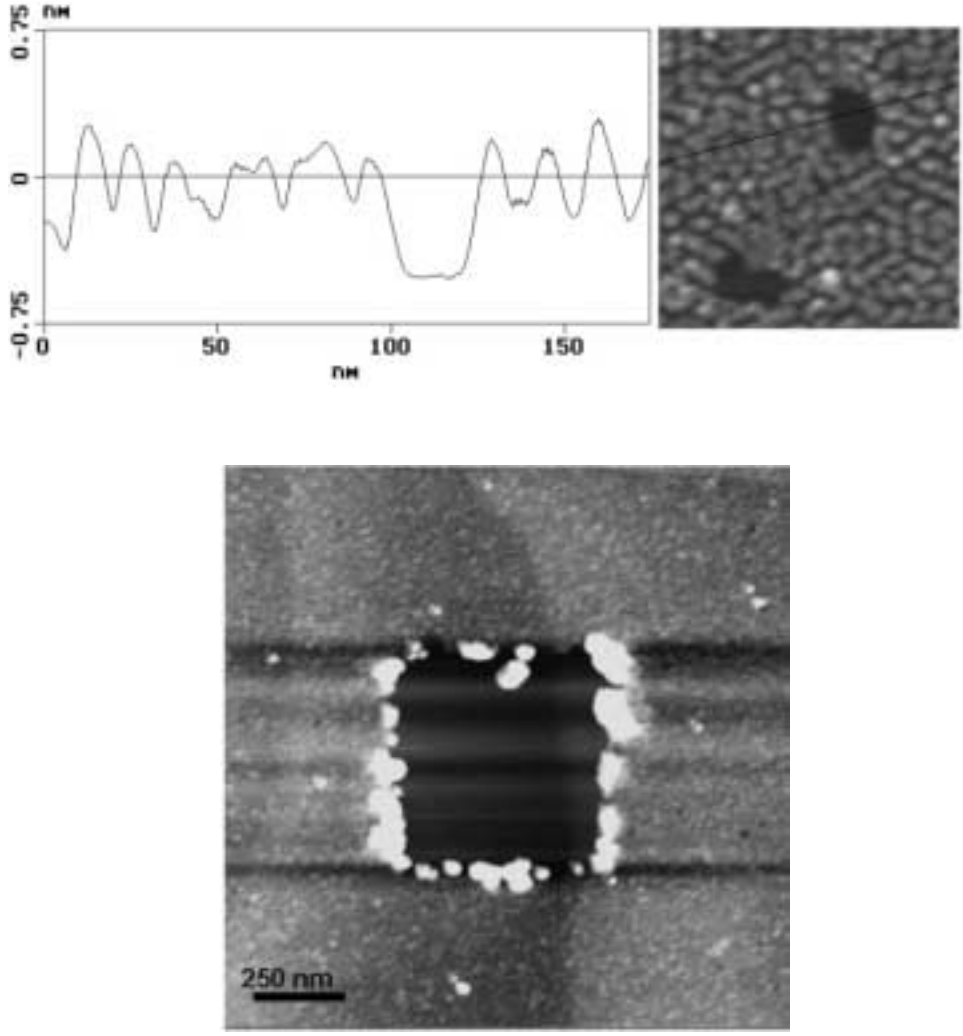

Figure 2.6: Top: Typical cross-section through a layer of $Td_{2,3}$-$(C_{12}H_{25})_{16}$ at 20 µg/ml concentration on graphite (see Sect. 3.1.1). Bottom: Tapping mode image (1.5×1.5 µm; scale bar 250 nm) of a layer of $Td_{2,3}$-$(C_{12}H_{25})_{16}$. The square in the middle was scratched free by imaging that area 5 times in contact mode with a force of ≈ 200 nN. The bright spots around the square are the material that has been scratched away.

2.4 Ellipsometry

The thickness of samples was also determined by ellipsometry. There, monochromatic laser light with a wavelength λ and known polarization is directed under an angle φ on a

surface of interest. The polarization state is characterized by a particular phase and amplitude relationship of the two components of the electric light vector parallel and perpendicular to the plane of incidence. The changes of the incoming light caused by optical and geometrical properties of the sample result in the characteristic angles, Δ and Ψ, measured in ellipsometry. Δ is defined by $\Delta = \delta_1 - \delta_2$, where δ_1 is the phase difference between the parallel component and the perpendicular component for the incoming wave and δ_2 is the same difference for the outgoing wave. Ψ reflects the change for the amplitude and is defined as $tg\Psi = \left|R^P\right| / \left|R^S\right|$, where R^P and R^S are the total reflection indices for the parallel and the perpendicular component of the polarised light. After a calibration of the ellipsometer in order to distinguish the contribution of the substrate and the one of the polymer film, the thickness of the polymer film can be calculated from the measured values of Δ and Ψ. The ellipsometer used was the type ELX-1, DER-Dr. Riss Ellipsometerbau GmbH, operating at λ=632.8 nm and at fixed angle of incidence $\varphi=70^{\circ}$. Knowing the refractive and the absorption index for graphite (n_g=2.55 and k_g=1.42) we calculated the thickness of the adsorbed layers assuming the refractive index of polystyrene (n=1.6) for the dendrimer layer. If we change n by 0.1, the derived thickness should have an error of ≈14%. We could not use the Ψ value because it varied too weakly as a function of the thickness for our system. Even if the value from ellipsometry presented big errors (see next Chapter), they agree with the thickness values measured with the AFM.

3 Experiments on structure formation of alkylated dendrimers on graphite

In the following Sections I am going describe the lateral organisation for the different dendrimers on the basal plane of graphite depending on the concentration of the solution. Additionally the kinetics and thermal stability of the observed structures will be checked. The solvent utilised was dichloromethane; the parameter utilized for the spin coating are described in Sect. 2.2.

3.1 Layers of $Td_{2,3}$-$(C_{12}H_{25})_{16}$

3.1.1 Concentration dependence

Three different concentrations of the solution were analysed (2 µg/ml, 20 µg/ml and 200 µg/ml).

2 µg/ml: Three different types of packing structures were observed. One of the most remarkable structures was regions covered by parallel rows of 5.4±0.7 nm spacing ("nanorods" or type A structure) (Figure 3.1). The lateral spacing was measured from a two-dimensional fast Fourier transform plot (2DFFT) that consists of two spots aligned in a straight line. The direction of the line is perpendicular to the direction of the rods in the real space. Usually type A regions were elongated along the rows. The regions tended to align parallel or at angles of 60° or 120° with respect to each other, probably due to the underlying graphite lattice. Typically, the regions were 50 to 100 nm wide and 70 to 800 nm long. In addition, we observed extended diffuse regions (type B). These diffuse regions were not bare graphite but were covered with a relatively homogeneous layer of dendrimers. Minor parts of the surface were covered with a worm-like structure (type C, Figure 3.2). The distance between neighbouring "worms" was roughly 11 nm. The lateral

spacing was deduced from the distance between neighbouring stripes. Note that the spacing is not a function of the tip shape (as mentioned in Sect. 1.4). The area fraction covered by type A, B, and C structures varied from sample to sample.

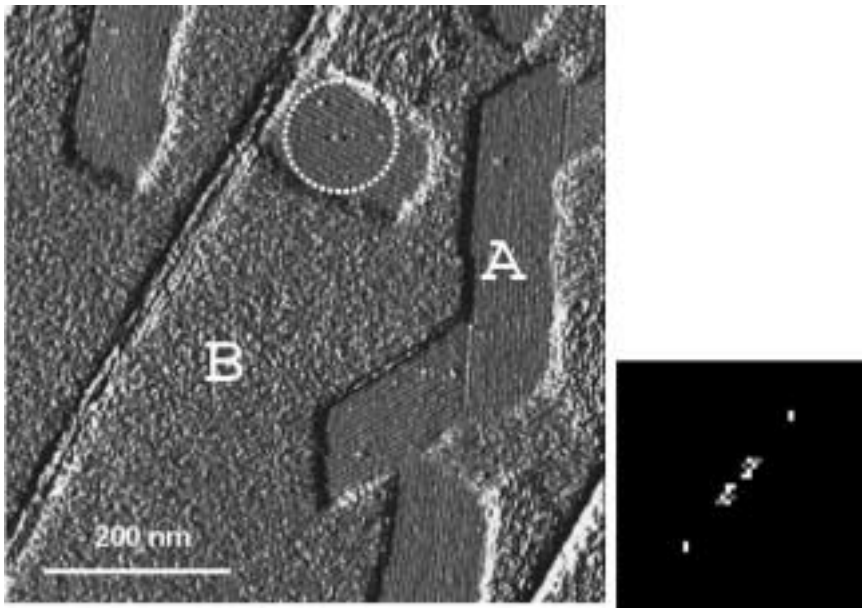

Figure 3.1: Amplitude image (scan size 639 nm) of a $Td_{2,3}$-$(C_{12}H_{25})_{16}$ layer on HOPG. The lines on the left part and on the right bottom part of the images represent steps of the graphite substrate. The letters "A" and "B" indicate the nanorods and the diffuse structure respectively. Right image: Fourier transform from the circled region in the image, it reflects the orientation of the rods and gives the values of their lateral spacing.

20 µg/ml: Here, two different kinds of packing structures were observed (Figure 3.2). Roughly 90% of the surface was covered by stripes or worm-like structures of 11 nm spacing (type C), as found from low concentrated samples. The stripes showed a tendency to orient parallely 0°, 60° or 120° with respect to each other. They seemed to consist of rows of dendrimers arranged in a zigzag (Figure 3.2, bottom, right). A two-dimensional fast Fourier transform (2DFFT) shows six reflexes at angles of 60°±4° corresponding to a distance of 6.0±0.2 nm. This indicates that at average the dendrimers are located at the sites of a hexagonal lattice with a lattice constant of (6.9±0.3) nm = 6.0 nm/sin60°. The area per unit cell of the hexagonal lattice is 41 nm^2. Hence, each unit cell probably contains one molecule. The maximal area occupied by one dendrimer can be estimated from the diameter of a molecule (4.5 nm) plus twice the length of a fully stretched dodecyl chain (1.5 nm) leading to a total maximal diameter of 7.5 nm. At hexagonal close packing circles of diameter 7.5 nm would occupy an area of 49 nm^2. This value agrees with the area of the unit cell taking into account that the alkyl chains of neighbouring dendrimers might

interdigitate. The remaining 10% of the surface was covered with a completely homogeneous layer (type D) of constant height. Only few holes were observed. Hence, the dendrimers form an almost pinhole free layer.

In order to explain why zigzag arrangement of molecules, which at first sight do not show a periodic ordering, lead to an hexagonal lattice in the 2DFFT, an argument similar to the reasoning in X-ray crystallography can be used. Sharp reflexes are obtained in X-ray diffraction patterns of crystals although the individual molecules thermally fluctuate [72]. Quantitatively, this is included in the Debye-Waller factor. In our case the dendrimers also "fluctuate" around their lattice sites, not in time but in space. Each dendrimer might be displaced from his lattice site but at average they form a hexagonal lattice. A simple mathematical treatment is described in the Appendix.

The measured values of the thickness were 0.8±0.2 nm from the cross section, 0.7±0.3 nm from the scratch and 1.5±0.2 nm from ellipsometry (see Figure 2.6). The diameter of the polyphenylene dendrimers, as obtained from computer simulations, was 4.5 nm. Hence, the results indicate that the dendrimers change their tetrahedral shape when adsorbing to graphite and probably are "flattened" on the surface.

200 µg/ml: Preparing samples from very high concentrated solutions we obtained layers with a granular structure where no individual dendrimers could be identified and no regular structures were observed. The thickness of the layers varied from 3 to 5 nm as determined from scratching an area free of polymer and measuring the height difference between the layer and the substrate (image not shown here).

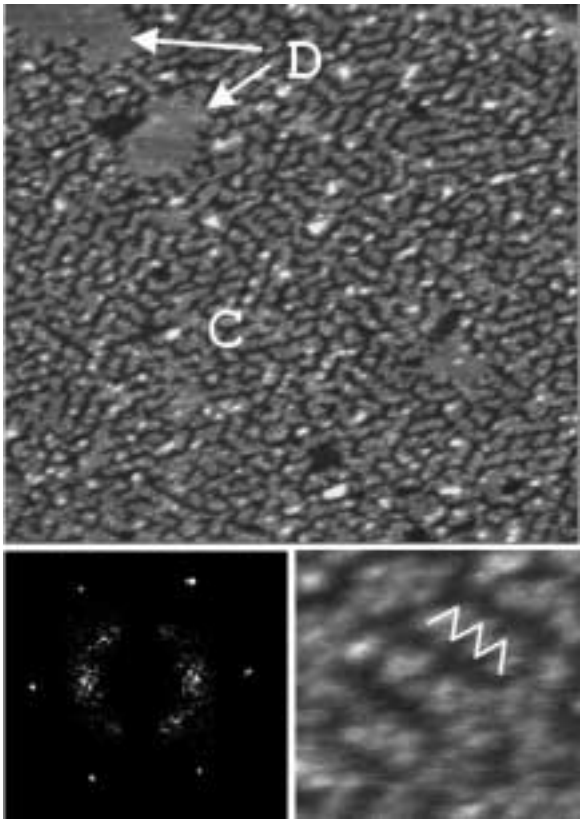

Figure 3.2: Top: Topographic image of $Td_{2,3}$-$(C_{12}H_{25})_{16}$ monolayer on HOPG prepared from a 20 μg/ml solution. Image size: 410×410 nm^2. Light areas are higher than dark regions. The letters "D" and "C" indicate the homogeneous layer and the (stripped) structure. Bottom: Detail scan (51×51 nm^2) of C region (right); two-dimensional Fourier Transformation of a C region (left).

3.1.2 Stability of the structures

We wanted to check the stability of the worm-like structure from 20 μg/ml concentrated sample. This was done by observing the samples over long time intervals, changing the temperature (annealing) and changing ambient condition, solvent and substrate.

The worm-like structure formed just after the spin coating. With time, we observed local rearrangement of the dendrimer inside the zig-zag (Figure 3.3). On the time scale required to take an image (typically 10-20 min) stripes disintegrated into more circular blobs and the individual blobs realigned into new stripes. This change in structure was not necessarily accompanied by a long-range lateral diffusion of the individual dendrimers. It merely reflects that a dendrimer that was positioned between two neighbours shifted from one neighbour to the other one. Hence, the dendrimers are in a dynamic equilibrium.

By additional annealing of the sample, we made sure that the worm-like structure is in equilibrium. The samples were annealed at temperatures from 90 to 100 °C for 30 min in a ventilated oven.

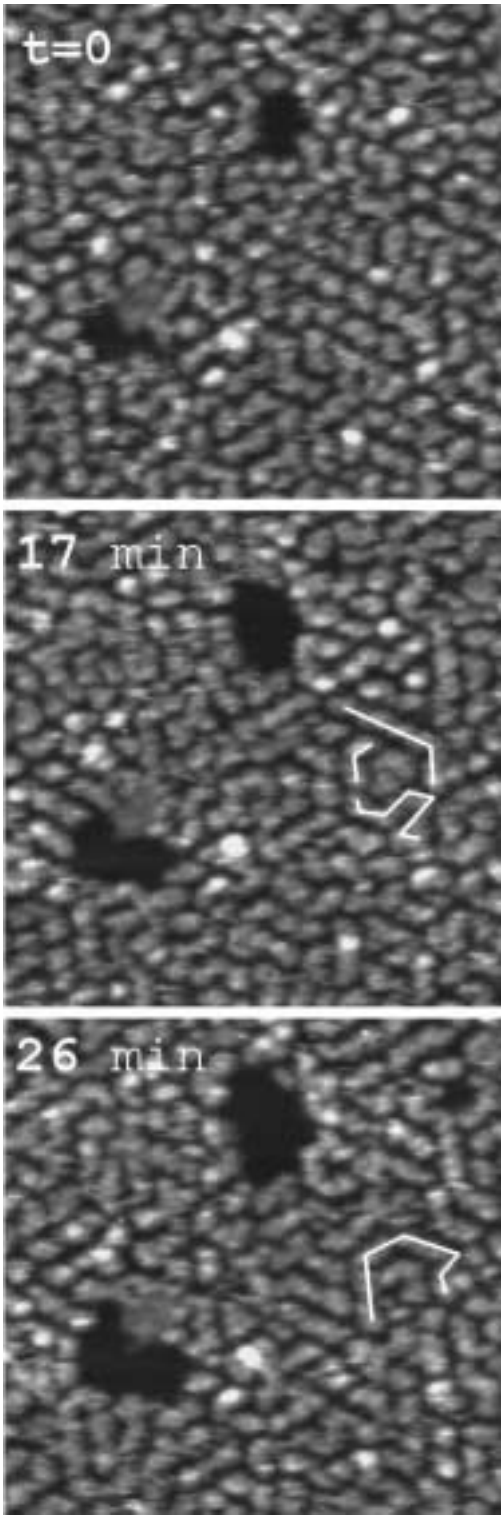

Figure 3.3: Sequence of images (200×200 nm) of $Td_{2,3}(C_{12}H_{25})_{16}$ dendrimers layer on graphite prepared from a 20 μg /ml dichloromethane solution. The lines indicated changes between the last two images.

In order to investigate the effect of the environment, we prepared layers on graphite, imaged the worm-like structure in air, and subsequently imaged the samples in ethanol in contact mode. The images showed that the molecules were able to regain the three-dimensional shape with the alkyl chains fully stretched and to assume an average height of roughly 7 nm (Figure 3.4, top). Probably ethanol competes for binding sites to the graphite and it is a solvent for the dendrimers $Td_{2,3}$-$(C_{12}H_{25})_{16}$. Both effects weaken the adsorption of dendrimers to graphite. These experiments showed that the worm-like structure is in equilibrium since the dendrimers could form it again after ethanol evaporation.

In order to check the effect of the solvent, dichlorobenzene instead of dichloromethane was utilised and the solution was spin coated on graphite and imaged in air. The sample consists of clusters of a defined height (≈5 nm) and the rest of the graphite surface was covered with a homogeneous diffuse layer (Figure 3.4, centre). A possible interpretation of the images is that the solvent can adsorb stronger to the graphite than the dendrimers and hinder the formation of an ordered dendrimer layer. The structure and the height of the clusters did not change even after annealing the sample at 150°C for 30 min.

When utilising a freshly cleaved sheet of mica as substrate, the layers consisted of clusters roughly 5 nm high (Figure 3.4, bottom). The value of the height was in good agreement with the simulated diameter of the polyphenylene core of the dendrimers (4.5 nm); this indicated that the dendrimers did not flat down on mica. The interaction between dendrimer and mica is probably less strong than between two dendrimers so they prefer to stick one to the other instead of distribute uniformly on the surface. On the top of the cluster we could observe a granular structure but the molecules did not arrange in any ordered structure.

Reassuming, these experiments showed that the worm-like structure is in equilibrium. It is specific for the images in air (which is representative for gaseous environment), for dichloromethane solution and for the graphite. The structure formation depends on the competitive interaction between dendrimer-substrate, dendrimers-solvent and solvent-substrate.

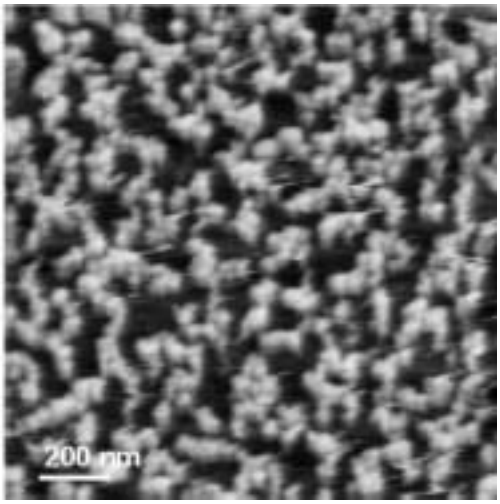

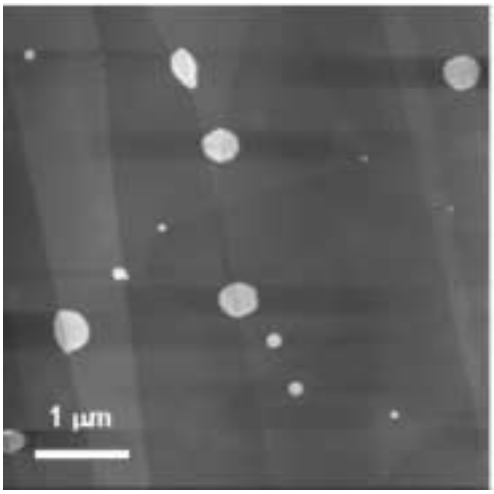

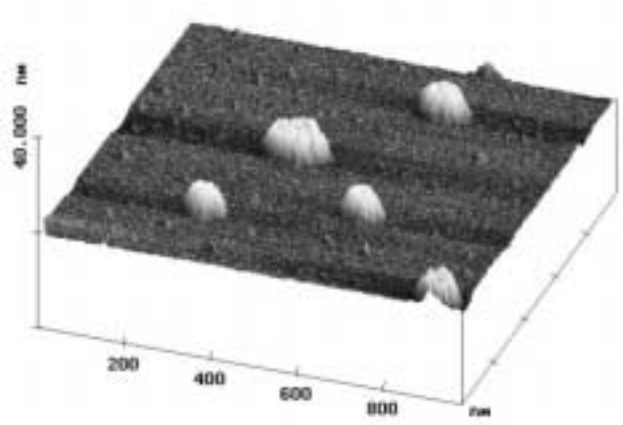

Figure 3.4: Top: Contact mode image (1.4×1.4 µm^2) taken in ethanol of a $Td_{2,3}$-$(C_{12}H_{25})_{16}$ layer on HOPG at 20 µg/ml. The sample was prepared as usual and then immersed in ethanol. Centre: topographic image of a sample prepared from a 20 µg/ml solution of $Td_{2,3}$-$(C_{12}H_{25})_{16}$ dissolved in dichlorobenzene on graphite (5×5 µm^2; scale bar 1µm). The sample consisted of clusters of defined height and a diffuse layer was covering the rest of the surface. Bottom: Three-dimensional representation of a topography image (978×978 nm^2 scan size) from a layer of $Td_{2,3}$-$(C_{12}H_{25})_{16}$ on mica. The average height of the clusters is 5 nm.

3.2 Layers of $Td_{1,4}$-$(C_{12}H_{25})_{16}$

Dendrimers $Td_{1,4}$-$(C_{12}H_{25})_{16}$ differ from $Td_{2,3}$-$(C_{12}H_{25})_{16}$ for the position of the alkyl chains: In $Td_{2,3}$-$(C_{12}H_{25})_{16}$ the chains are attached on the "surface" of the polyphenylene core while in $Td_{1,4}$-$(C_{12}H_{25})_{16}$ they are located more inside the polyphenylene core.

Samples prepared from low concentrated solutions (2 μg/ml) of $Td_{1,4}$-$(C_{12}H_{25})_{16}$ showed regions covered with parallel rows of 5.7±0.5 nm spacing (type A) and regions covered with a diffuse layer (type B) (Figure 3.5, left). When preparing samples from a higher concentrated solution (20 μg/ml) we observed a uniform layer with only a few holes (Figure 3.5, right). In the layer, it was possible to distinguish single molecules since the dimension of one spot was roughly 5 nm. However, the molecules did not form ordered structures. The clear distinction between an inner phenylene core and an outer alkyl shell that characterised $Td_{2,3}$-$(C_{12}H_{25})_{16}$ is probably important for the formation of hexagonal packing. The thickness of these layers was 0.8±0.2 nm from the cross section, 0.7±0.3 nm from the scratch, and 1.5±0.2 nm from the ellipsometry. Since these values are considerably smaller than the diameter of the molecule, the dendrimers are flatten on the surface. Thus the positions of the alkyl chains did not influence the flattening of the molecules on the surface.

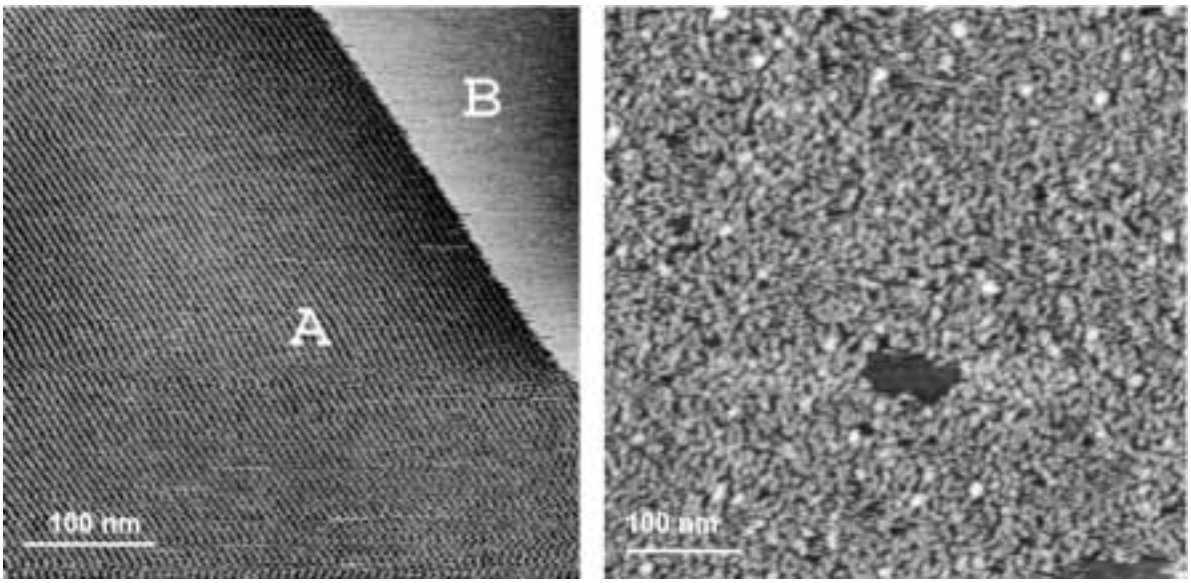

Figure 3.5: Left: Topographic image of a monolayer of $Td_{1,4}$-$(C_{12}H_{25})_{16}$ on graphite prepared from low concentration solution (2 μg/ml). Image size 438×438 nm. The periodicity of the nanorods is 6 nm (type A). Diffuse regions (type B) are also present. Right: the layers from 20 μg/ml concentrated solution consist of a monolayer with defects. Image scan size: 500×500 nm^2.

3.3 Layers of $Tri_{2,3}$-$(C_{12}H_{25})_{16}$

The $Tri_{2,3}$-$(C_{12}H_{25})_{16}$ dendrimer with its central benzene group has a planar, propeller-like shape with a height of roughly 2 nm as deduced from computer simulations.

Layers from very dilute solutions (1 μg/ml) showed regions with nanorods and diffuse regions (image not shown here). The lateral spacing between the rods was 5.9±0.2 nm.

When preparing samples from a low concentrated solution (2 μg/ml) of $Tri_{2,3}$-$(C_{12}H_{25})_{16}$ dendrimer, a two-dimensional crystals were formed in 50% of the experiments (Figure 3.6, left). We determined the lattice constants as described before [71]. The primitive unit cell is a rombohedral one with the lattice constants a=7.4±0.4 nm, b=10.1±0.3 nm and an angle of 121°±2°. Note that in the crystals each protrusion has an elongated, oval and not spherical shape. Crystals were oriented parallel 0°, 60° or 120° with respect to each other indicating that the underlying graphite determines their orientation. The area of a unit cell is 63 nm^2. The calculated diameter of a molecule is 6.9 nm (3.9 nm core plus 3 nm from the dodecyl alkyl chains) that leads to a value of the area per molecule of 41 nm^2. From the mismatch between the measured and the calculated area value, we can conclude that each protrusion corresponds to two tightly aggregated dendrimer rather than a single one. The pairs form two-dimensional crystal. Geometrically this is possible because the diameter of 6.9 nm is an upper limit for the molecular dimension on the surface.

In some experiments (13%) we observed also rod formation (Figure 3.6, right) with the same periodicity as from 1μg/ml concentrated sample. 37% of the samples did not show any ordered pattern.

Samples from higher concentrated solutions (>10 μg/ml) showed the formation of disordered monolayers similar to Figure 3.3, right (images not shown here). The thickness of these layers was 0.9±0.2 nm from the cross section, 1.1±0.3 nm from the scratch, and 1.7±1.1 nm from the ellipsometry. The thickness does not deviate significantly from the calculated height of the molecule of 2 nm. The dendrimer, with its central benzene group, has a more planar shape and the height, deduced from the space filled model, comes from the twisted benzene rings in each arm.

The two-dimensional crystals from $Tri_{2,3}$-$(C_{12}H_{25})_{16}$ dendrimers at 2 μg/ml concentrated solution were stable and could be scanned many times. We observed, however, changes in the period of time required to take an image (Figure 3.7): crystalline regions could shift

from one place to another, some changed their shape and the molecules inside of one region could change the orientation.

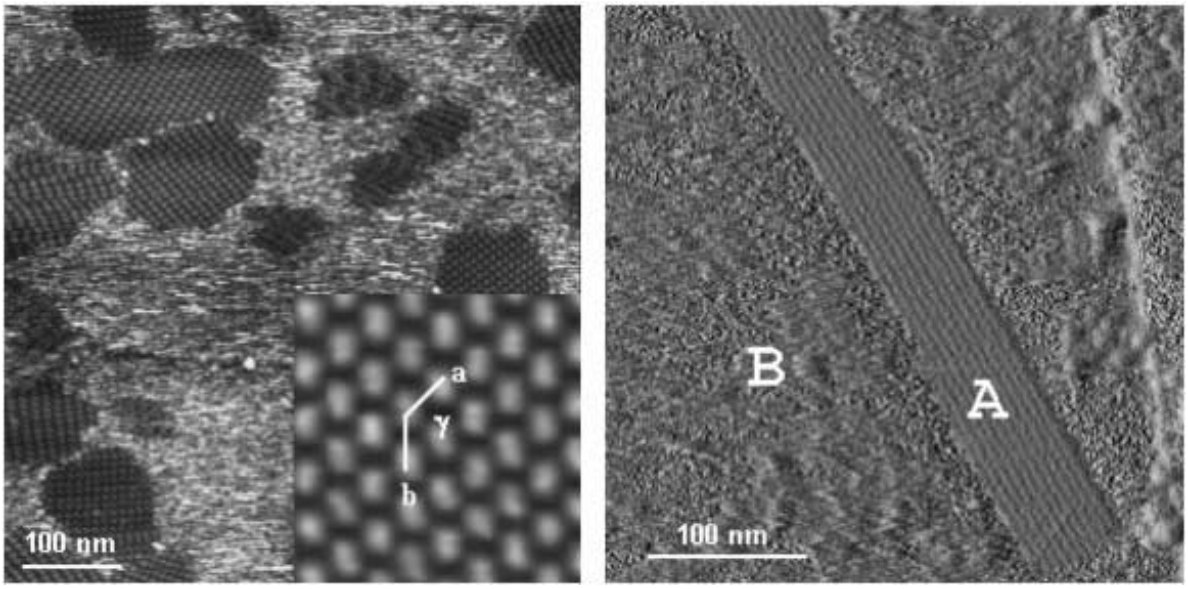

Figure 3.6: Left: Topographic image (580×580 nm^2) of $Tri_{2,3}$-$(C_{12}H_{25})_{16}$ layer formed from 2 µg/ml concentrated dichloromethane solution. The molecules form two-dimensional crystals. The inset (70×70 nm^2) shows the crystal lattice in detail, including the lattice vectors. Right: amplitude image of 360×360 nm^2 scan size. A region consisting of parallel rows with a spacing of 6 nm can be seen.

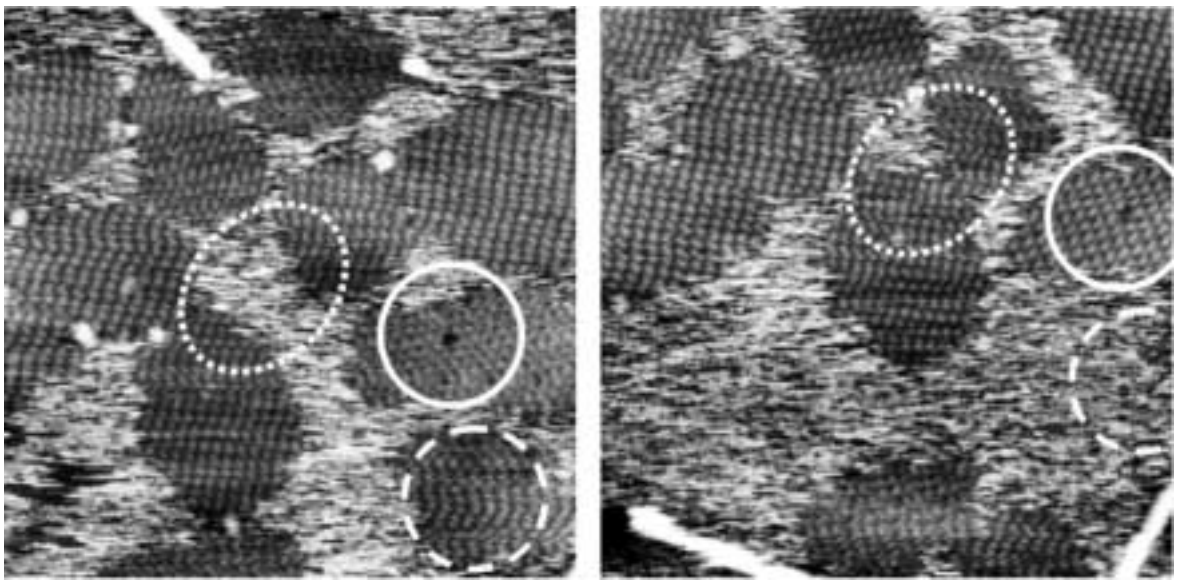

Figure 3.7: Two subsequent images (340×340 nm) of $Tri_{2,3}(C_{12}H_{25})_{16}$ dendrimer layer prepared from 2 µg/ml solution. The circle shows the same areas on the sample from one scan to the other. The relative position of one region to the other, shape, and size of crystalline areas have changed.

3.4 Layers of $TriN_{2,3}$-$(C_{12}H_{25})_{16}$

In $TriN_{2,3}$-$(C_{12}H_{25})_{12}$ the core unit is a nitrogen molecule with three attached phenyl rings. The overall shape is pyramidal and the diameter of the molecule without alkyl chains is 4.4 nm. Layers obtained from 5 and 10 μg/ml concentrated solution showed regions with two-dimensional crystals (type E), regions with parallel rods (type A) and diffuse regions (type B) (Figure 3.8, left). A 2DFFT in the type E regions gave a rombohedral lattice with average values of the lattice constants a=(6.5±0.4) nm and b=(6.3±0.2) nm and with an angle of 82.0°±5.7°. The corresponding area per unit cell was 40 nm^2. Each unit cell contained one molecule. By adding the diameter of 4.4 nm to twice the length of a dodecyl chain we obtain a value of 7.4 nm. In a hexagonal closed-packed structure this would lead to a value for the area per molecule of 47 nm^2. This agrees with the area per unit cell also considering a possible interdigitation between the external alkyl chains. In type A regions, the lateral spacing between the rods was 5.1±0.3 nm. The value of the spacing calculated from the experiments with 5 μg/ml concentrated solution and the ones from the experiments with 10 μg/ml concentrated solution were the same within the experimental error. The thickness of the regions with the two dimensional crystals and that one of the regions with the rods was roughly 0.5 nm, measured from the diffuse regions.

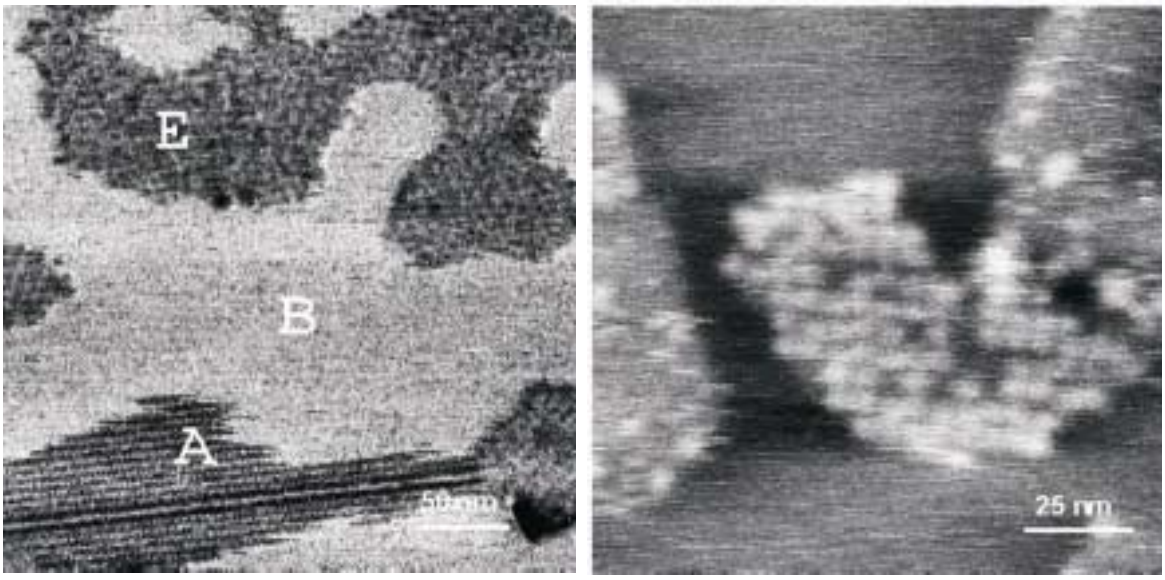

Figure 3.8: Sample obtained from 5 μg/ml concentrated solution from the TriN-dendrimers. Left: phase image of 320×320 nm scan size. The letters "B" and "A" indicates the diffuse and the rods regions respectively. The letter "E" indicates the two-dimensional crystals that are shown in detail on the right image (134×134 nm scan size).

Just after spin coating $TriN_{2,3}$-$(C_{12}H_{25})_{16}$ from 5 and 10 μg/ml concentrated solution, the layers consisted almost completely of diffuse regions. Waiting some hours it was possible to distinguish between the diffuse regions and the freshly formed regions with the two-dimensional crystals. The nanorod region appeared 24 hours after the preparation of the sample. Since the extension of the regions with the two-dimensional crystals did not change significantly, probably the formation of the rods occurred from dendrimers from the diffuse regions.

3.5 Layers of tetrahedral dendrimers with alkoxy chains of different lenght

In order to analyze the influence of the substituted akyl chains, dendrimers $Td_{2,3}$-$(OC_{12}H_{25})_{16}$, $Td_{2,3}$-$(OC_8H_{17})_{16}$, and $Td_{2,3}$-$(OC_5H_{11})_{16}$ were investigated. They all resemble $Td_{2,3}$-$(C_{12}H_{25})_{16}$ except that the alkyl chains are attached via an ether group and their length was different: Dodecyl chains in $Td_{2,3}$-$(OC_{12}H_{25})_{16,}$ octyl chains in $Td_{2,3}$-$(OC_8H_{17})_{16}$, and pentyl chains in $Td_{2,3}$-$(OC_5H_{11})_{16}$.

When preparing layers from these dendrimers, the samples were stored overnight in a vacuum chamber.

$\underline{Td_{2,3}\text{-}(OC_{12}H_{25})_{16}}$: With samples from low concentrated solutions (2 μg/ml) we observed the nanorod regions (type A), oriented parallel (0°), 60° or 120° with respect to each other and with (5.7±0.4) nm spacing (Figure 3.9). Increasing the concentration of the solution to 20 μg/ml, we obtained layers with granular structure with distinguishable molecules with different shape and diameter ranging from 3 to 6 nm. Thus there was not obvious ordered structure, compared to the already presented ones. The layers were similar to Figure 3.5, right (image not shown here).

$\underline{Td_{2,3}\text{-}(OC_8H_{17})_{16}}$: Samples from 2 μg/ml concentrated solution showed regions with nanorods (Figure 3.10, left). The lateral spacing was (5.6±0.3) nm. The regions with nanorods were not stable from one scan to other and they could shift or change their dimension. Layers from high concentrated solution (20 μg/ml) showed different kinds of packing structures (Figure 3.10, right). Most of the surface was covered by granular regions roughly 1 nm high (type F). Nanorods regions formed between some of the granular regions. The lateral periodicity of the rods was (5.2±0.1) nm and the regions were oriented reflecting the three-fold symmetry of the graphite. The width of the nanorod

regions ranged from 50 to 200 nm and the length from 100 to 300 nm. The rest of the surface was covered by a diffuse layer (type B). Unlike the regions with nanorods from dilute solution samples, the rods were stable and easily detectable on the surface. From cross sections of the images (Figure 3.11), one could recognise the different kinds of structures.

$Td_{2,3}$-$(OC_5H_{11})_{16}$: Layers obtained from dendrimers with the shorter alkyl chains, from 2 μg/ml concentrated solution, showed only the formation of a diffuse layer (type B). The samples obtained from 20 μg/ml concentrated solution showed the same packing structures as samples from $Td_{2,3}$-$(OC_8H_{17})_{16}$ similar to Figure 3.10 (images not shown here). The lateral periodicity between the rods was (5.4±0.1) nm.

In Table 3.1 the values of the lateral periodicity between the rods for the dendrimer with different alkyl chain length are listed. The length of the chains seems not to influence the periodicity. Considering fully stretched alkyl chains, the difference between the diameter of $Td_{2,3}$-$(OC_{12}H_{25})_{16}$ and $Td_{2,3}$-$(OC_5H_{11})_{16}$ dendrimer should be 1.6 nm while the measured values of the lateral spacing were the same within the error.

The concentration of the solution at which nanorods form, depends on the alkyl chain length. For the $Td_{2,3}$-$(OC_{12}H_{25})_{16}$ dendrimer, the rod formation occurred only from diluted solution; for the $Td_{2,3}$-$(OC_8H_{17})_{16}$ dendrimer, rods formed from diluted and concentrated solution while for the $Td_{2,3}$-$(OC_5H_{11})_{16}$ dendrimer they form only from concentrated solution.

The thickness of the layers from 20 μg/ml concentrated solution was measured only from cross sections of the images. Since the maximum measured values were roughly 1 nm, the dendrimers probably became flat on the graphite surface and lost the tetrahedric shape.

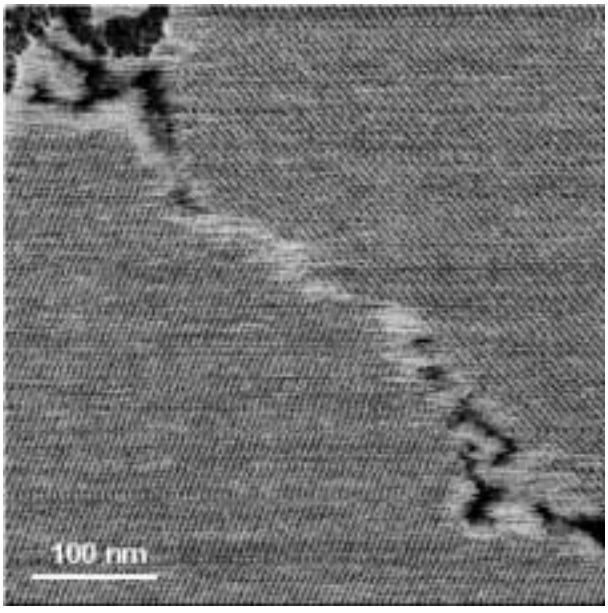

Figure 3.9: Phase image of 500×500 nm scan size; samples from 2 μg/ml concentrated solution of $Td_{2,3}$-$(OC_{12}H_{25})_{16}$ showed regions with parallel rods. Here is shown a boundary between two regions oriented at 60° one respect to each other.

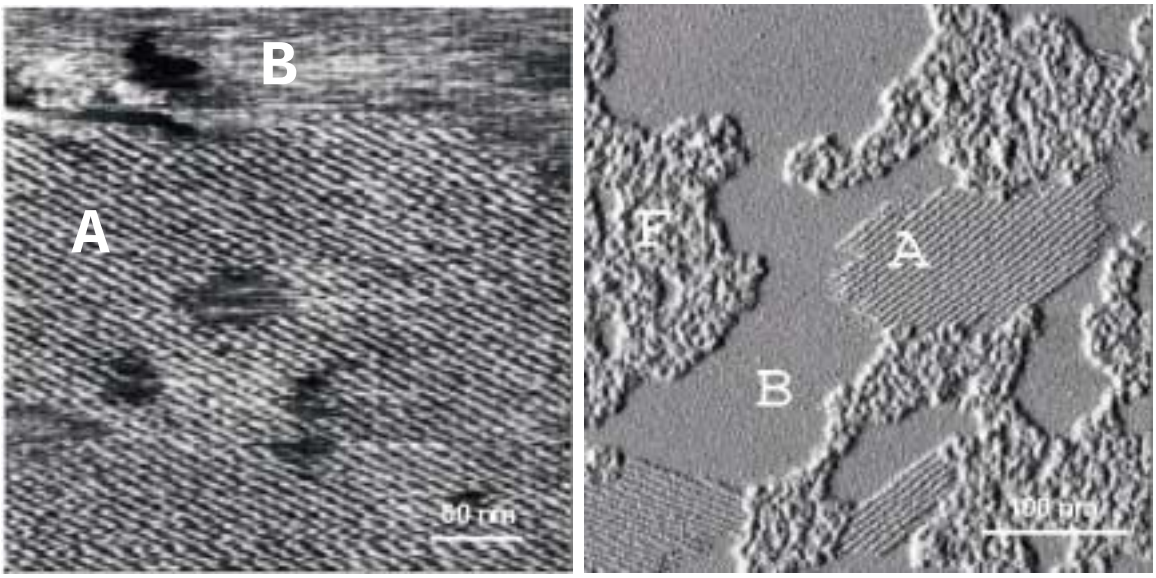

Figure 3.10: Left: Topographic image (310×310 nm^2 scan size) of a $Td_{2,3}$-$(OC_8H_{17})_{16}$ dendrimer from 2 μg/ml concentrated solution. The regions with the rods (A) are not stable and difficult to image. Right: Amplitude image (400×400 nm^2 scan size) of a sample from 20 μg/ml. The letters "B", "A" and "F" indicate diffuse layers, regions with nanorods and granular structure regions, respectiverly.

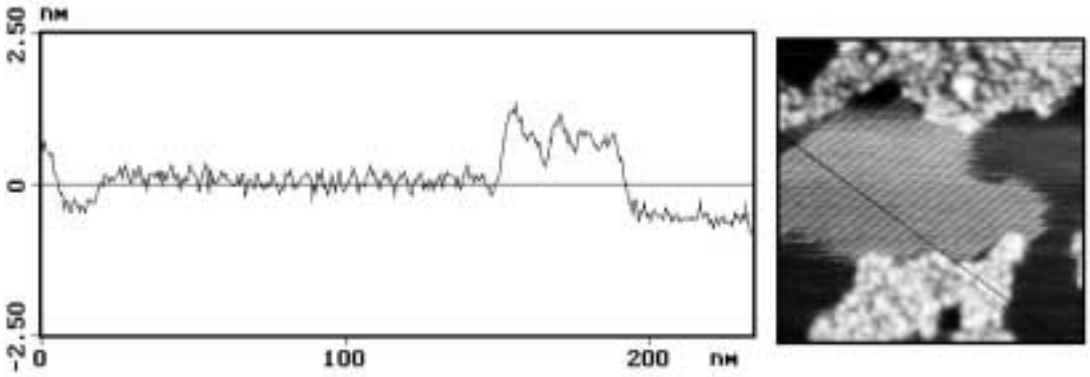

Figure 3.11: Cross section through a layer of $Td_{2,3}$-$(OC_8H_{17})_{16}$ dendrimer from 20 μg/ml concentrated solution. Regions with clusters (type F), regions with nanorods (type A) and the diffuse layer were easy to distinguish.

Dendrimer	Concentration [μg/ml]	Rods spacing [nm]
$Td_{2,3}$-($OC_{12}H_{25}$)$_{16}$	2	5.7±0.4
$Td_{2,3}$-(OC_8H_{17})$_{16}$	20	5.2±0.1
$Td_{2,3}$-(OC_8H_{17})$_{16}$	2	5.6±0.3
$Td_{2,3}$-(OC_5H_{11})$_{16}$	20	5.4±0.02

Table 3.1: **Lateral spacing between the nanorods for alkoxy-terminated dendrimers with different alkyl chain length, at different concentration of the solution.**

We monitored the evolution of the samples with time. Between one measurement and the other the tip was withdrawn from the surface in order to avoid any possible influence of the tip during the repeated scans. We observed that layers evolved to a more ordered phase. An example of a change towards a more ordered structure is shown in Figure 3.12. $Td_{2,3}$-(OC_8H_{17})$_{16}$ and $Td_{2,3}$-(OC_5H_{11})$_{16}$ dendrimers showed just after the spin coating of a 20 μg/ml an unstructured layer, covering almost the whole surface. After one to three hours, the first granular structures appeared on the surface. After waiting typically 12 hours, the distinction between diffuse and granular regions was evident. The formation of the two regions was not influenced by the humidity; the same features were obtained storing the samples overnight in a vacuum chamber. Then regions with parallel rods started to grow (Figure 3.13, top, left) from the granular regions and grew within two hours (Figure 3.13, top, right). They appeared in different positions on the surface and they covered roughly 10% of the surface. Since the neighbouring regions with clusters did not change in shape and size, the dendrimers nanorods grew from the diffuse regions.

In layers from $Td_{2,3}$-(OC_8H_{17})$_{16}$ dendrimers from more diluted solutions (2 μg/ml) we observed that the regions with rods changed their orientation (Figure 3.13, bottom). When neighbour regions had different orientation of the rods, the smaller regions disappeared and the bigger regions increased.

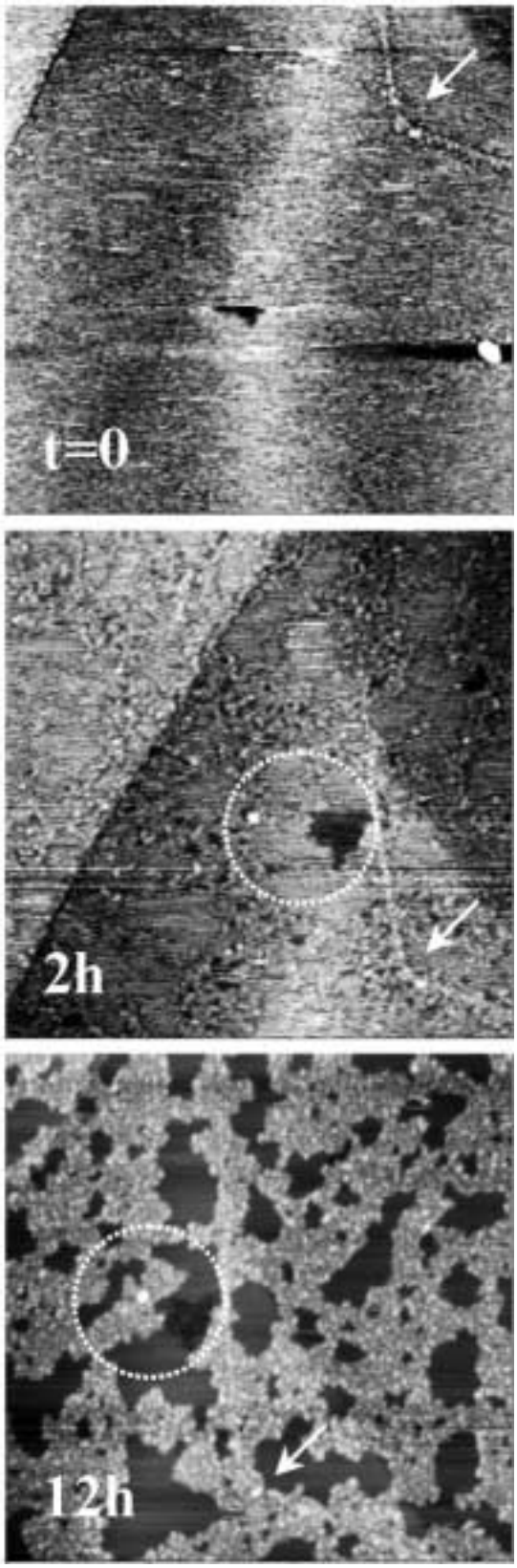

Figure 3.12: Time sequence on the same area (700×700 nm^2 scan size) on a layer from $Td_{2,3}$-$(OC_8H_{17})_{16}$ solution (20 μg/ml). The features indicated by the circle and the arrows (3D-aggregates, defects) made sure to find again the same area on the surface after several hours.

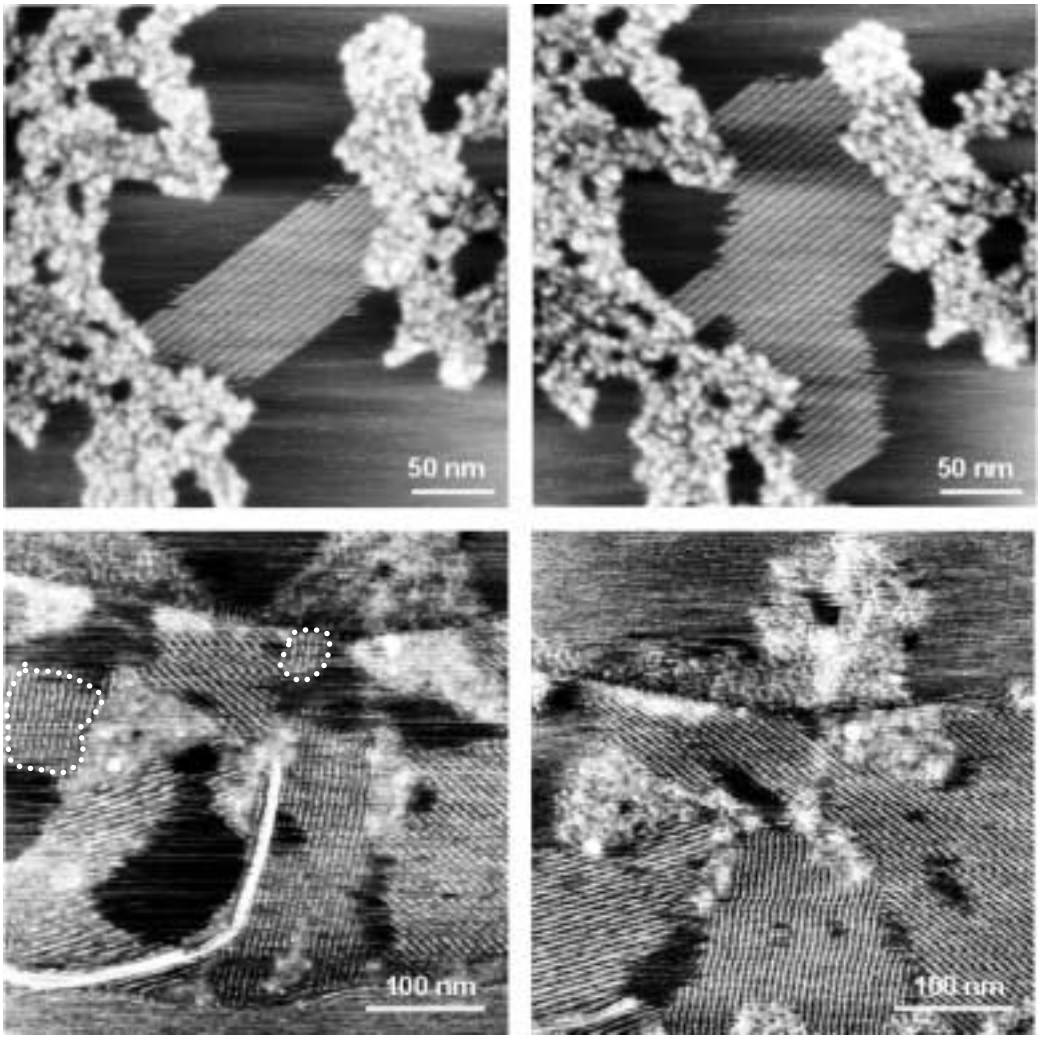

Figure 3.13: Topographic images of layer from $Td_{2,3}$-$(OC_8H_{17})_{16}$ dendrimers after waiting 12 hours after the sample preparation. The images on the right side were taken two hours after the correspondent images on the right side. Top: layer from 20 μg/ml concentrated solution (scan size 308×308 nm^2). Bottom: layers from 2 μg/ml concentrated solution (the scan size was 426×426 nm^2). The two dashed regions on the left image disappear and the bigger 3 regions on the bottom grow after 2 hours.

When annealing freshly prepared samples from $Td_{2,3}$-$(OC_8H_{17})_{16}$ and $Td_{2,3}$-$(OC_5H_{11})_{16}$ dendrimers, we observed the formation of diffuse and granular structure (Figure 3.16). Layers from $Td_{2,3}$-$(OC_8H_{17})_{16}$ annealed roughly 14-18 hours after the spin coating (see previous Figure 3.13, top, right) were thermodynamically stable. In particular, the regions with the nanorods neither disappeared nor increased.

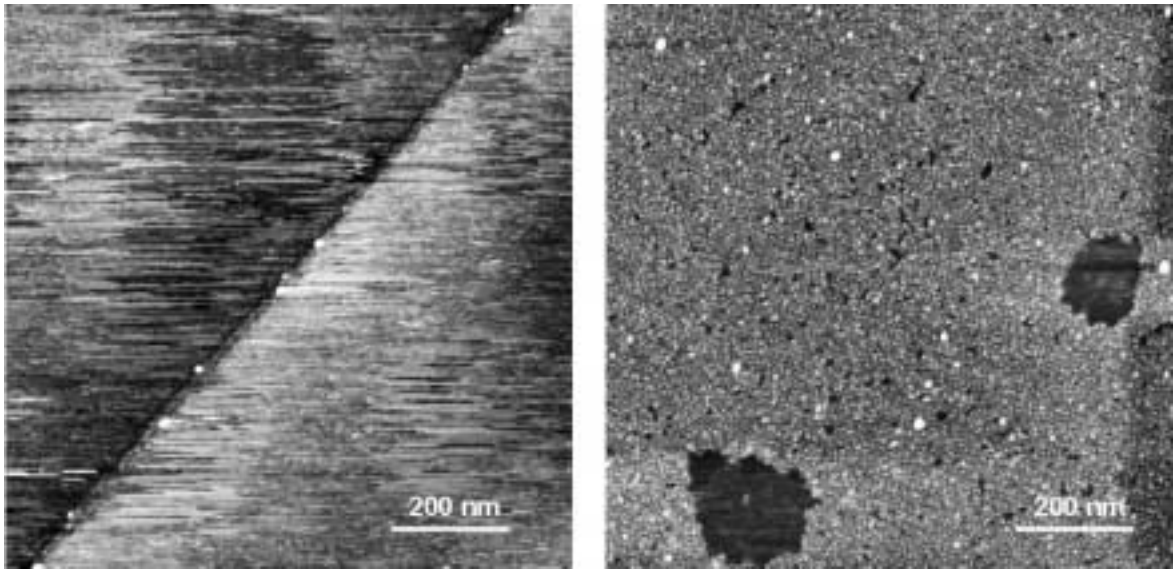

Figure 3.16: Images of a sample from $Td_{2,3}$-$(OC_8H_{17})_{16}$ solution (20 µg/ml) before (left) and after annealing the sample at 90°C for 30 min (right) (scan size: 963×963 nm^2). The images are taken at different points on the same sample due to annealing without sample contact.

3.6 Needle-like objects

In roughly 5% of the all experiments we observed the formation of an additional ordered structure. In monolayers of $Td_{2,3}$-$(C_{12}H_{25})_{16}$, $Td_{2,3}$-$(OC_{12}H_{25})_{16}$, $Td_{2,3}$-$(C_5H_{11})_{16}$ and $Tri_{2,3}$-$(C_{12}H_{25})_{16}$ dendrimers, we observed isolated "sticks" or needle-like objects with height from 1 to 2 nm and width from 15 to 39 nm (values listed in Table 3.4) (Figure 3.17). The needles laid on the top of another dendrimer layer and not directly on graphite. We were unable to resolve smaller features within the needles. The needles were oriented parallel, 60° or 120° with respect to each other; they were observed on annealed samples or on samples prepared 12 hours before.

As seen in Sect. 1.4, the shape of the tip can affect the profile of objects on a surface. In this case, when the tip scans over a single sharp feature, the value for the width is increased. A sketch is shown in Figure 3.18. With a tip radius of 30 nm, for example, imaging a sharp feature 1 nm high, could give origin to a profile 15 nm wide. Without knowing the real profile of the tip is not possible to deconvolute the image. Hence, the measured width is a maximum value for the real width of the features. The height of the structure increases with the distance from the graphite. If the needles consist of dendrimers, we would conclude that withdrawing from the substrate the dendrimers tend to regain their 3D-shape.

Dendrimer	Concentration [μg/ml]	Height [nm]	Width [nm]
$Td_{2,3}$-$(C_{12}H_{25})_{16}$	20	1.5±0.2	14.9±2.3
$Td_{2,3}$-$(C_{12}H_{25})_{16}$	2	0.5±0.1	33.3±2.6
$Td_{2,3}$-$(OC_{12}H_{25})_{16}$	2	0.8±0.2	16.6±4.3
$Td_{2,3}$-$(OC_5H_{11})_{16}$	2	1.9±0.2	17.8±1.0
$Tri_{2,3}$-$(C_{12}H_{25})_{16}$	2	1.8±0.6	39.4±3.3

Table 3.4: List of the measured values of the height and width of the sticks for different dendrimers. The errors are the standard deviation from different images from the same experiment

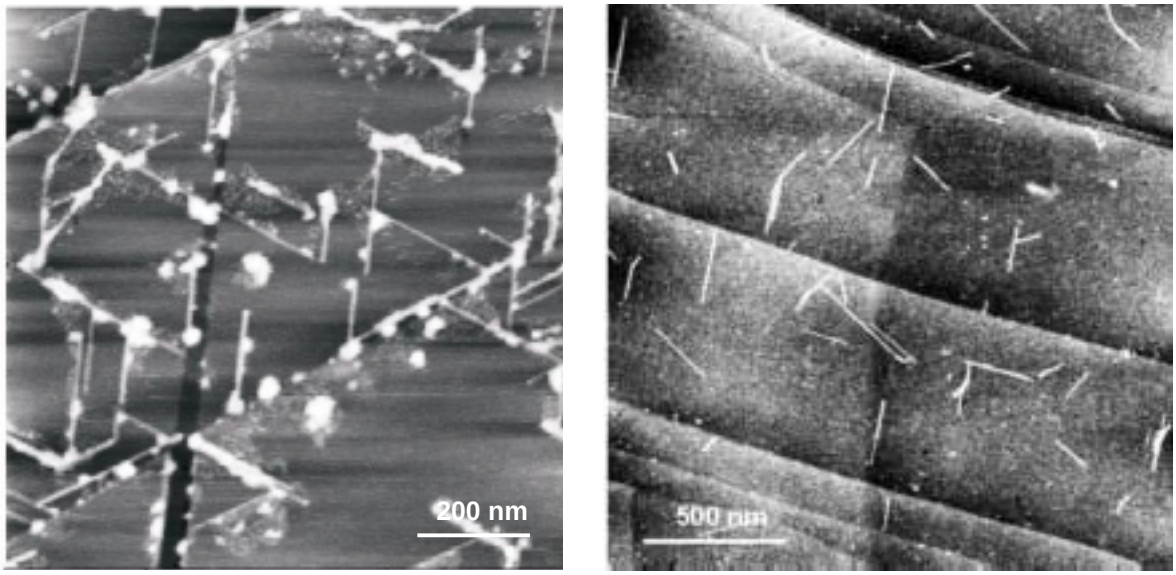

Figure 3.17: Left: Image of a $Td_{2,3}$-$(OC_{12}H_{25})_{16}$ layer from a 2 μg/ml concentrated solution (1μm×1μm scan area). The sample was imaged after storage overnight in vacuum. The angle between the sticks was roughly 60° and they lay on the top of a diffuse layer. Right: Large-scale tapping mode image (2×2 μm^2) of a layer of $Td_{2,3}$-$(C_{12}H_{25})_{16}$ prepared from a dichloromethane solution (20 μg/ml) after annealing the sample at 96°C for 30 min. The needles lay on the top of a worm-like structure.

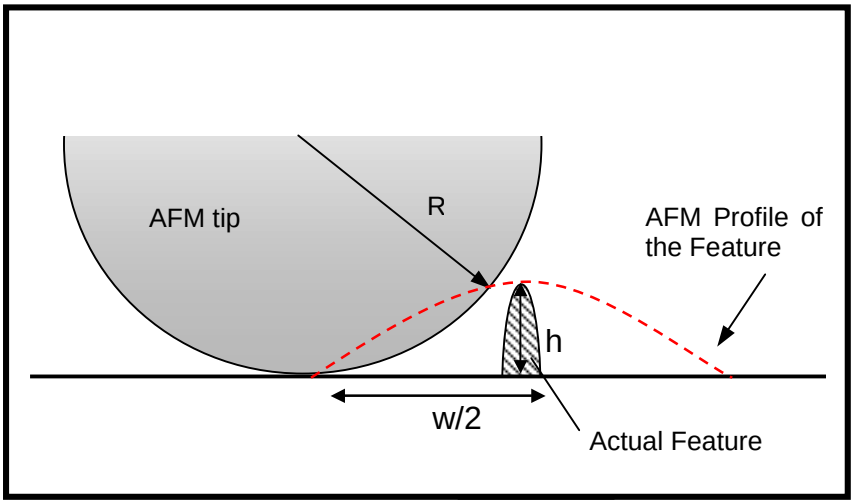

Figure 3.18: Sketch of an AFM tip scanning over a sharp feature. The AFM profile is broader than the actual feature. The tip apex radius, *R*, and the height, *h*, and width, *w*, of the feature are related by the relation:

$$w = 2\sqrt{2Rh - h^2}$$

4 Interpretation of structure formation

4.1 Classification of two-dimensional structures

The typical structures observed for dendrimers on graphite can be classified in three types: Granular regions, diffuse regions, and nanorods.

1. In granular regions individual molecules could usually be identified. The molecules are tightly packed without long-range order. Within these regions no reorganization of the individual dendrimers was observed with time, at least not during several days. Thus, granular regions resemble the structure of a two-dimensional glass. One exception was observed with the $Td_{2,3}$-$(C_{12}H_{25})_{16}$ dendrimer. Here the "granular" packing structure has an average hexagonal order (Sect. 3.1.1).
2. In diffuse regions no individual molecules could be detected and the structure resembles that of a gas or liquid phase. A two-dimensional gas should fill the whole free surface area while for a two-dimensional liquid one could expect to see holes only occasional (like a three-dimensional liquid is characterized by an own volume and can fill only a part of a three-dimensional defined space). We did observe holes that were roughly 0.3 nm deep. They were, however, so rare and small that it was impossible to exclude the possibility that surface contamination prevented dendrimers to occupy these areas even when being in a gaseous state. Therefore, we cannot unambiguously decide whether the diffuse regions represent a two-dimensional gas or liquid. In any case, diffuse regions were not bare graphite but were covered with a relatively homogeneous layer of dendrimers.
3. "Nanorod" regions consisted of parallel stripes that had a periodicity of 5.1-5.9 nm (Table 4.1). Usually, nanorod regions were elongated along the rows. They tended to align parallel or at angles of 60° or 120° with respect to each other, reflecting the three-fold symmetry of the underlying hexagonal graphite lattice. A direct comparison with the orientation of the underneath graphite lattice is not possible since in tapping mode atomic resolution is not obtained. To change from tapping mode to contact mode involves the substitution of the cantilever and thus the loss of

correlation with the observed nanorod region. Nanorods formed from low concentrated solutions (from 1 to 2 μg/ml) were not as stable as the ones formed from high concentrated solutions (from 10 to 20 μg/ml). In the lower concentrated samples, the regions change slightly in dimension from one scan to the other and they could shift or the nanorods inside them could change their orientation (see Figure 3.12). In the higher concentrated samples the nanorods appeared stable and the lateral distance was slightly smaller. For $Td_{2,3}$-$(OC_8H_{17})_{16}$ for instance the spacing was (5.2±0.2) nm for layers formed from 20 μg/ml concentrated solution. It increased to (5.6±0.3) nm for layers formed from 2 μg/ml concentrated solutions. This may reflect a higher 2D density of molecules in the surrounding diffuse layer.

The categorization of the two-dimensional dendrimers structures on graphite into three different phases (granular, diffuse, and nanorods) is in general valid. For dendrimers with three arms ($Tri_{2,3}$-$(C_{12}H_{25})_{12}$ and $TriN_{2,3}$-$(C_{12}H_{25})_{12}$) we observed one additional structure, i.e. the regions with two-dimensional crystals that correspond to rombohedral lattices (see Figure 3.6 and 3.8). Obviously, the two-dimensional crystals are a characteristic of dendrimers with three-fold symmetry. However a missing sub-molecular resolution hinders us to understand how the different core unit determine the ordered structure.

The time scale for crystal growth after deposition (~1h) is different from the one for growth of the nanorods (~12h). This indicates different formation kinetics or just smaller activation energy.

4.2 Influence of the solution concentration

One motivation for these studies was to find out under which conditions nanorods form.

Nanorods tended to form preferentially when both phases, the granular and the diffuse phase, were present and coexisted. This was largely determined by the bulk concentration of the solution. At high concentration the whole surface was covered with a granular structure. At low concentration no coverage at all or diffuse regions were observed. As one example the surface coverage for the granular structure Θ_{gr} of $Td_{2,3}$-$(OC_8H_{17})_{16}$ vs. the concentration is shown in Figure 4.1. The surface coverage is the surface area covered by the granular structure divided by the total surface area imaged. It was determined from many AFM images of several samples.

To compare the adsorption of different dendrimers on graphite we fitted the surface coverage $\Theta_{gr}(c)$ with a Langmuir adsorption isotherm: $\Theta_{gr} = \left(1 + c_{50}/c\right)^{-1}$. Here, c_{50} is the concentration at which 50% of the surface is covered by the granular structure. It also serves as a guideline to choose the best concentration for nanorod formation. For practical reasons we did not directly determine the surface coverage of nanorods versus concentration: Nanorods usually covered only 5-20% of the surface even under optimal conditions. Therefore, the errors would be large. Langmuir isotherms were chosen for their simplicity. We did not have a specific adsorption process in mind and the fit merely serves to obtain c_{50} as a measure for the adsorption strength and speed. Values of c_{50} for the different dendrimers are listed in Table 4.1.

The concentration c_{50} is correlated with estimated adsorption energy (Figure 4.2). To estimate the adsorption energy E_{ad} we summed up the number of methylene units, n_{CH2}, and the number of methyle groups of each dendrimer and multiplied it with the adsorption energy of a methylene unit on graphite of 7 kJ/mol [73]: $E_{ad} = \left(n_{CH2} + n_{CH3}\right) \cdot 7 kJ/mol$. The concentration required to achieve 50% granular structure decreases with increasing E_{ad} in the range from 500 to 1000 kJ/mol. When adding the adsorption energy of the phenylene units (roughly 15 kJ/mol [74]) the same tendency is observed, i.e. the value of c_{50} decreases with E_{ad}. The reason is probably that the surface coverage increases with the adsorption energy since under the experimental conditions the adsorption time was constant.

For dendrimers with an E_{ad} above 1000 kJ/mol, i.e. for dendrimers with more than ≈130 methyl/methylene units, the adsorption energy seems to be so high that the amount adsorbed after a given time is limited by another process such as diffusion/transport to the surface.

With increasing concentration the dendrimers are packed more densely as indicated by the favoured formation of the granular structure compared to the diffuse structure. Thus, the granular structure is likely to have the highest surface density (molecules per unit area), the nanorod structure has an intermediate surface density, and the diffuse structure is expected to have the lowest surface density. This is confirmed by an independent observation. When taking cross-sections through images that show at least two structures in one image, the granular structure was always thicker than the nanorod structure and the nanorods regions were thicker than the diffuse structure (Figure 3.11). This indicates that dendrimers are distorted the more densely they are packed assuming a nearly constant volume density of the dendrimers.

The area fraction of the nanorods is not only a function of the area fraction of the granular structure and the diffuse layer, which would be maximum for c_{50} , but also of the length of the perimeter of the granular structure. Thus, to get reasonable amounts of nanorods on the surface one should choose the bulk concentration around c_{50}.

Dendrimer	Spacing (nm)	c_{50} (µg/ml)	E_{ad} (kJ/mol)
$Td_{2,3}$-$(C_{12}H_{25})_{16}$	5.4 ± 0.7	6	1344
$Td_{1,4}$-$(C_{12}H_{25})_{16}$	5.7 ± 0.5	10	1344
$Tri_{2,3}$-$(C_{12}H_{25})_{12}$	5.9 ± 0.2	7	1088
$TriN_{2,3}$-$(C_{12}H_{25})_{12}$	5.1 ± 0.3	9	1088
$Td_{2,3}$-$(OC_5H_{11})_{16}$	5.4 ± 0.3	27	560
$Td_{2,3}$-$(OC_8H_{17})_{16}$	5.4 ± 0.3	12	896
$Td_{2,3}$-$(OC_{12}H_{25})_{16}$	5.7 ± 0.4	8	1344

Table 4.1: Periodicity of nanorods of dendrimers on graphite. The periodicity is the average of samples prepared from different concentrations. Listed are furthermore the concentration of the dichloromethane solution at which half the surface is covered by the granular structure c_{50}, and the hypothetical adsorption energy E_{ad}.

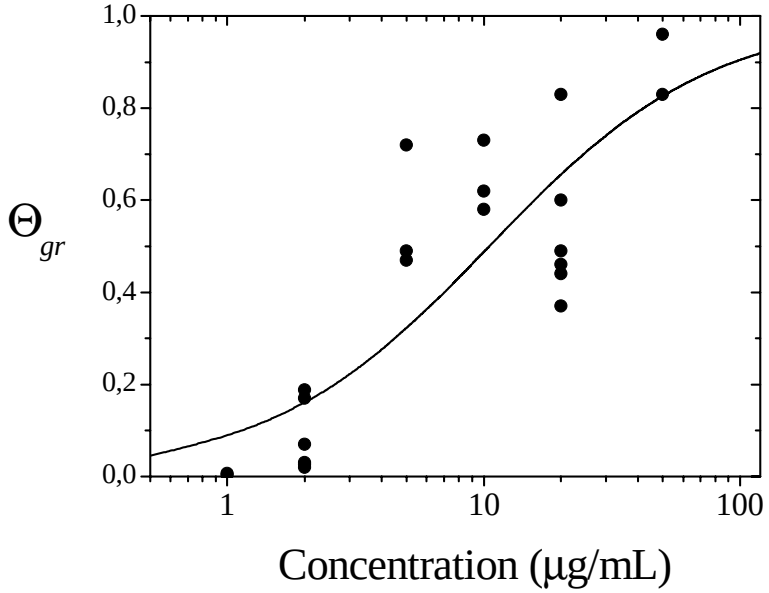

Figure 4.1: Relative surface area Θ_{gr} covered by granular regions of $Td_{2,3}$-$(OC_8H_{17})_{16}$ from CH_2Cl_2 on graphite versus the concentration of the solution. The areas were determined from AFM images on different places and preparations roughly 20 h after deposition. Each symbol is the result of one experiment. The continuous line represents a fit with the Langmuir adsorption isotherm. Such fits were used to determine the concentration of half coverage c_{50}.

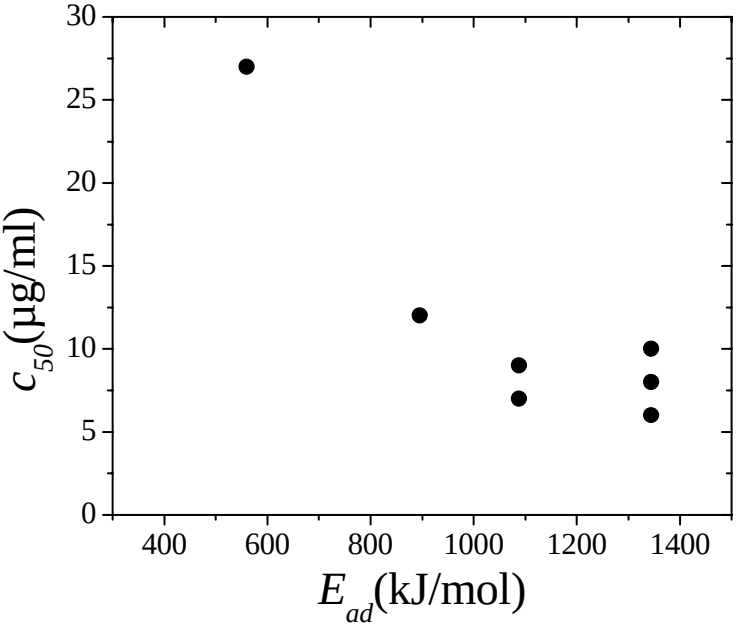

Figure 4.2: Concentration of half coverage c_{50} versus the hypothetical adsorption energy.

4.3 Thickness of the layers

The measured thickness values show that the dendrimers change their shape when adsorbing to graphite. The tetrahedral shape is lost and the dendrimers lay flat on the surface. This result disagrees with the expectation to have shape persistent nanoparticles due to the dense packing of benzene rings within the molecule. For the dendrimer to lay flat on the surface the central tetrahedral core should lay flat on the surface with the 4 arms at 90° one from the other. The energy required to obtain a quadratic planar phenyl coordinated C atom is supposed to be 600-700 kJ/mol [75]. From MM2 simulation (Molecular Mechanic, version 2), we calculated that, between the stable planar and the stable tetrahedric conformation there exists another stable conformation in which the central C atom forms a "pyramid" with the 4 phenyl rings with a C-C-C angle of about 85° (Figure 4.3). The energy difference between the tetrahedral and the "pyramidal" shape is roughly 280 kJ/mol. In a MM2 simulation, it is possible to take a 3D shape of a molecule and find out how much potential energy is associated with that shape. Molecules tend towards their minimum energy shapes, when no thermal excitations or external forces are present. The MM2 simulation is valid if there are no changes of the electronic configuration of the molecule. Note that corresponding to this conformation, the four oligophenylene arms of the dendrimer should lay flat on the surface.

Another possibility for the flattening of the tetrahedral dendrimer is that the central core is still tetrahedral, three oligophenylene arms lay on the surface and the fourth one is bent

towards the surface. This requires energy because oligophenylene chains are relatively stiff. A rough estimate for the bending energy for an oligophenylene chain can be obtained from the *worm-like chain* model (WLC) [79]. This model assumes that the value of the bond angles is fixed and a segment is free to rotate around the bond direction (i.e. a crossing between the segments of a chain is not allowed) (Figure 4.4).

Knowing the contour length of a chain L (the length of the macromolecule measured along its backbone from atom to atom) and the persistence length l_p[1], the bending energy E_b can be estimated from [80]:

$$E_b = k_B T \left(\frac{R_e}{R} \right)^2 \qquad (4.1)$$

where $R_e = \sqrt{2Ll_p}$ is the end-to-end distance of a chain and R is the bending radius of the coil. The measured value of the persistence length for a polyester chain is 10.7 nm [81]. Calculating L from the length of the C-C bonds and the diameter of the benzene ring, assuming $R \approx L/2$, E_b is roughly 100 kJ/mol.

A rough estimate for the adsorption energy of a dendrimer can be obtained summing up the adsorption energy of the single alkyl chains and of the benzene rings on graphite. A single dodecyl chain has an adsorption energy of ≈80 kJ/mol [73]. The match between the alkane's C-C-C zigzag (0.251 nm) and the spacing between "holes" in the graphite lattice (0.246 nm) is mainly responsible for the high affinity of alkanes on graphite [82]. Even considering that the first few methylenes next to the phenylene moiety are sterically hindered to bind directly to the graphite, the adsorption energy of the alkyl chains of one of the four arms of a dendrimer is roughly 200 kJ/mol. In addition, each phenylene ring contributes an adsorption energy of about 15 kJ/mol [74]. If it lays flat on the graphite, each arm has an adsorption energy in the order of 400 kJ/mol. Such a high available energy could be enough to deform the molecule changing its tetrahedral core unit or bending the oligophenylene arms. Concluding, there is no theoretical evidence for one of the two models.

[1] The sum of the projections of the bonds onto the unit vector of the polymer chain; the unit vector of the polymer chain is the vector of the first bond divided by the bond length. Essentially l_p describes how far the polymer extends in a given direction before becoming a random coil.

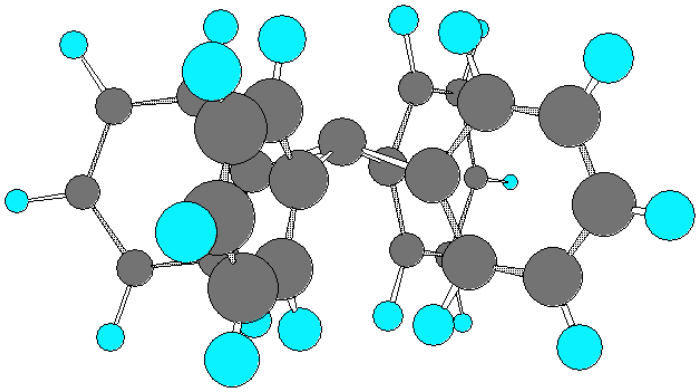

Figure 4.3: Model of a "pyramidal" conformation for a tetraphenylmethane molecule.

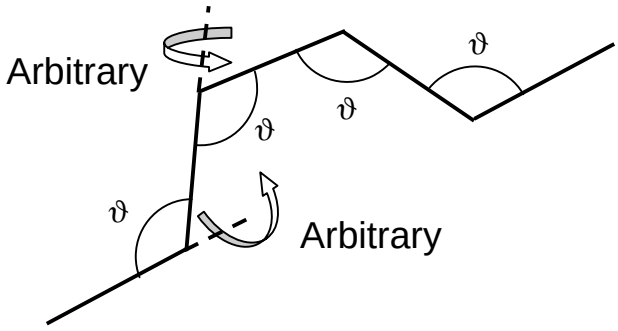

Figure 4.4: Description of the allowed rotations for a worm-like chain polymer.

4.4 Mobility of the dendrimers

In Ch. 3 changes of the two-dimensional structure with time have been described. In layers from $Td_{2,3}(OC_8H_{17})_{16}$, $Td_{2,3}$-$(C_5H_{11})_{16}$ and $TriN_{2,3}$-$(C_{12}H_{25})_{12}$ from 20 to 5 µg/ml concentrated solution, the regions evolved towards a more ordered phase and nanorods regions grew. The formation of nanorods seems due to condensation of dendrimers from diffuse regions into the two-dimensional ordered structure.

The growth of the nanorods could be dominated by different processes: Influence of the AFM tip; *reaction* control (desorption or adsorption, reorientation) or a *diffusion* control on the surface. Since the samples were observed after a given time without scanning, we can exclude that the AFM tip induces the crystallization of the dendrimers in the nanorods. An additional deposition of molecules to the surface is excluded since there is no supernatant

solution over the sample. Hence the dendrimers reorient or are diffusing laterally in order to form the nanorods. Since the density of molecules in the diffuse regions is unknown, it is not possible to distinguish unambiguously between the two processes. A diffusion process is likely because the sliding movement of alkyl chains and benzene parallel to a graphite surface has a negligible activation energy as compared to k_BT at room temperature [73,83,84]. This mobility could explain why the diffuse regions appear "fuzzy" under the AFM tip. The dendrimers could have high molecular mobility in the diffuse regions and they have to be stabilized in a monolayer in order to become visible for the AFM.

Samples from $Td_{2,3}$-$(OC_8H_{17})_{16}$ dendrimer from more dilute solution (2 µg/ml) showed the disappearance of small nanorod domains while neighbouring, larger domains grow. This phenomenon could be described by an Ostwald ripening process, during which the interline energy is minimized. The Ostwald ripening process was already observed in systems such as alkylated oligothiophene [85] and dendritic nanorods [15], both on graphite. In these systems the reorientation at the domain boundaries of the crystalline regions control the transformation.

4.5 Variation of the alkyl chain length

Comparing the lateral distance between the rods for samples from dendrimers with different length of the alkyl chains, we verified that the length of the alkyl chains did not influence the lateral spacing of the nanorods within an error of less than 0.4 nm. Considering fully stretched alkyl chains, the difference between the diameters of the $Td_{2,3}$-$(OC_5H_{11})_{16}$ and the $Td_{2,3}$-$(OC_{12}H_{25})_{16}$ dendrimer should be 1.7 nm. The question arises, where the additional part of the alkyl chains are positioned. One possibility is that they are not in direct contact with the graphite at all but that they lay on top of the dendrimers. This, however, is unlikely because the adsorption energy on graphite of the chains is high. Assuming that the additional parts of the alkyl chains are lying directly on the graphite, we have to conclude that they fill gaps along the nanorods (Figure 4.5). They are probably stretched parallel to the direction of the nanorods and interdigitate with the alkyl chains of the two neighboring dendrimers within a nanorod. A spacing of 5.5 nm could accommodate roughly 12 parallel alkyl chains (the distance between parallel alkyl chains was measured to be approximately 0.45 nm [82]). Considering that the number of

alkyl chains per molecule is 16 or 12, this suggests that each dendrimer has roughly half of the alkyl chain (8 or 6) on one side and half on the opposite side along a nanorod.

Probably by interdigitation they also gain van der Waals energy due to interaction with adjacent alkyl chains and this energy is bigger than the entropy loss due to the confinement.

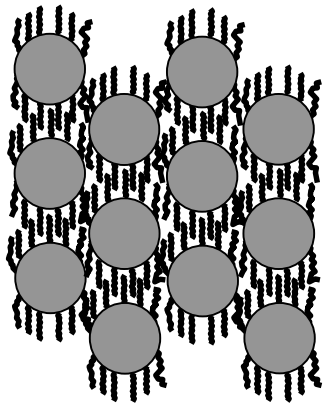

Figure 4.5: Schematic structure of alkyl substituted polyphenylene dendrimers on graphite. The alkyl chains are oriented parallel to the direction of nanorods.

Conclusions

AFM experiments have been made to characterise the morphology of alkyl substituted polyphenylene dendrimers on a solid substrate. In solution the dendrimers are regarded as shape persistent nanoparticles because of the very large number of rigid benzene rings within a defined space. On graphite they change their shape and flatten down on the surface to form ordered patterns. AFM experiments showed that thickness of a dendrimer monolayer correspond to one fifth of the diameter of a molecule in bulk. Ellipsometry measurements confirmed these results showing that the AFM probe does not significantly deform the sample during the scans.

The alkyl substituted polyphenylene dendrimers form nanorods, two-dimensional crystals, diffuse or granular structure. In the granular structure individual molecules can usually be identified but they do not show any long-range order. Nanorods form regions of different dimension where they lie one parallel to each other with a repeated spacing of 5.1-5.9 nm. To a large degree this is determined by the concentration of the solution applied. Diffuse regions form at low concentrations, granular regions at high concentrations and nanorods form preferentially at intermediate concentrations. In particular, the concentration at which the nanorods form decreases with the adsorption energy of the molecules.

These can be considered as self-assembled and supramolecular structures. They are “self-assembled” in the sense that they form patterns fast (within 1-5 s) and spontaneously even from low concentrated solutions and that they are stable. They are “supramolecular” in the sense that the structure is complex and not intuitively predictable like hexagonal close packing. To my knowledge this is the first observation of spontaneous rod formation of approximately spherical or circular macromolecules.

A prerequisite for the formation of ordered patterns is probably a lateral diffusion of the dendrimers or a reorientation. The kinetics of single alkyl chains and benzene rings on graphite has already been described in other works [73,83,84]. Experiments with dendrimers of different alkyl chain length indicated that the periodicity of the parallel nanorods is not affected by the length of the alkyl chains. Hence alkyl chains are mainly oriented parallel to the nanorods. The value of the lateral distance corresponds to the dendrimer having roughly half of the alkyl chain on one side and half on the opposite side along a nanorod. Thus, the presence of the nanorods is due to the specific molecular architecture of the dendrimers.

The ability of alkyl substituted polyphenylene dendrimers to form highly ordered structures might have applications on the design of new materials. In future works, we are going to examine the adsorption of partially functionalised dendrimers. In particular, we plan to leave one arm of the tetrahedral dendrimer without alky chains in order to find out how the thickness of the two-dimensional supramolecular structures is going to change. The determination of the diffusion coefficient of a dendrimer inside the diffuse layers could clear up the mechanism of the nanorod formation. By utilising molybdenum disulfide instead of graphite as a substrate one could investigate the influence of the lattice constant of the substrate on the periodic pattern.

Appendix

Two-dimensional Fourier transform of an AFM image expected from a hexagonal lattice with randomly displaced molecules

We first assume that each dendrimer has the same height and size in an AFM image. Hence, all dendrimers contribute equally to the two-dimensional Fourier transform (2DFFT) and the "scattering factor" f is the same for each dendrimer. This is not totally true. Even if all dendrimers have identical shapes in an AFM image they might appear differently. This difference is due to the tip influence. If a single molecule is imaged by an AFM tip its volume appears enlarged since the image is something like a convolution between tip and sample. If two dendrimers in contact are imaged the volume in the image is less than twice the volume of a single dendrimer because the enlargement is effective only on one side. This effect, that due to the tip shape neighboring dendrimers appear with a reduced volume, is neglected.

We consider the structure of dendrimers as described in Figure 3.19, (a). At average the dendrimers are positioned at a certain place in the hexagonal unit cell. This position is given by the two-dimensional vector $\vec{r}_0$. This vector goes from the origin of the unit cell to the mean position of the dendrimer. Each dendrimer is shifted by a discrete distance Δ towards one of its neighbors. The shift is directed along one of the six lattice axes. Though only a certain discrete shift distance is allowed the direction of the shift is supposed to be random, i.e. a shift along each of the six axis has the same probability.

The intensity of a reflex in the 2DFFT (corresponding to the scattering amplitude) is proportional to the square of the structure factor F_{hk}

$$I \sim \left|F_{hk}\right|^2$$

and the F_{hk} is given by

$$F_{hk} = \frac{f}{A} \cdot \exp\left(-i\vec{G}_{hk}\vec{r}\right)$$

A is the area of a unit cell. $\vec{G}_{hk}$ is the reciprocal lattice vector for the reflexes with Miller indexes h and k. With the unit vectors in real space $\vec{a}$ and $\vec{b}$ the unit vectors in reciprocal space, $\vec{A}$ and $\vec{B}$, are defined by

$\vec{A}\cdot\vec{a}=2\pi$, $\vec{A}\cdot\vec{b}=0$, $\vec{B}\cdot\vec{a}=0$, $\vec{B}\cdot\vec{b}=2\pi$

An AFM image typically contains 1000-10000 dendrimers. Hence, the 2DFFT averages over a large number of molecules. The average structure factor is

$$F_{hk}=\frac{f}{A}\cdot\left\langle\exp\left(-i\vec{G}_{hk}\vec{r}\right)\right\rangle$$

We assume that $\vec{r}=\vec{r}_0+\vec{u}$, with $|\vec{u}|=\Delta$. The direction of $\vec{u}$ is along one of the six lattice axes. Inserting leads to

$$F_{hk}=\frac{f}{A}\cdot\exp\left(-i\vec{G}_{hk}\vec{r}_0\right)\cdot\left\langle\exp\left(-i\vec{G}_{hk}\vec{u}\right)\right\rangle$$

We write the last factor in a series:

$$\left\langle\exp\left(-i\vec{G}_{hk}\vec{u}\right)\right\rangle=1-i\left\langle\vec{G}_{hk}\vec{u}\right\rangle-\frac{1}{2}\left\langle\left(\vec{G}_{hk}\vec{u}\right)^2\right\rangle\pm\ldots$$

The displacement in each of the six directions is random and not correlated with the reciprocal lattice vector. Hence, the second term is zero. For the last term we can write

$$\left\langle\left(\vec{G}_{hk}\vec{u}\right)^2\right\rangle=G_{hk}^2\cdot\left\langle u^2\right\rangle\cdot\left\langle\cos^2\varphi\right\rangle$$

Since the displacement is supposed to be discrete the second term is $\left\langle u^2\right\rangle=\Delta^2$. The angle φ is the angle included by the reciprocal lattice vector and $\vec{u}$. If the angle between say $\vec{a}$ and $\vec{G}_{hk}$ is denoted by φ_0 the angles with the other five axes are $\varphi_0+\pi/3$, $\varphi_0+2\pi/3$, $\varphi_0+\pi$, $\varphi_0+4\pi/3$, and $\varphi_0+5\pi/3$. Since a displacement in all six directions has the same probability we get

$$\left\langle\cos^2\varphi\right\rangle=\frac{1}{6}\left[\cos^2\varphi_0+\cos^2\left(\varphi_0+\frac{\pi}{3}\right)+\ldots+\cos^2\left(\varphi_0+\frac{5\pi}{3}\right)\right]=\frac{1}{2}$$

Hence, we obtain

$$\left\langle\exp\left(-i\vec{G}_{hk}\vec{u}\right)\right\rangle=1-\frac{1}{4}G_{hk}{}^2\Delta^2\pm\ldots$$

Using this expression, the intensity of one of the inner six reflexes (characterized by *h* and *k* = 1,0 or 0,1 or 1,1) is

$$I=I_0\cdot\exp\left(-2\pi^2\frac{\Delta^2}{a^2}\right).$$

with $I_0 = \left(\frac{f}{A}\right)^2$. The exponential factor corresponds to the Debye-Waller factor. Here, a is the lattice constant of the hexagonal lattice. In summary: The intensity of the inner spots decreases exponentially with the relative displacement Δ/a squared.

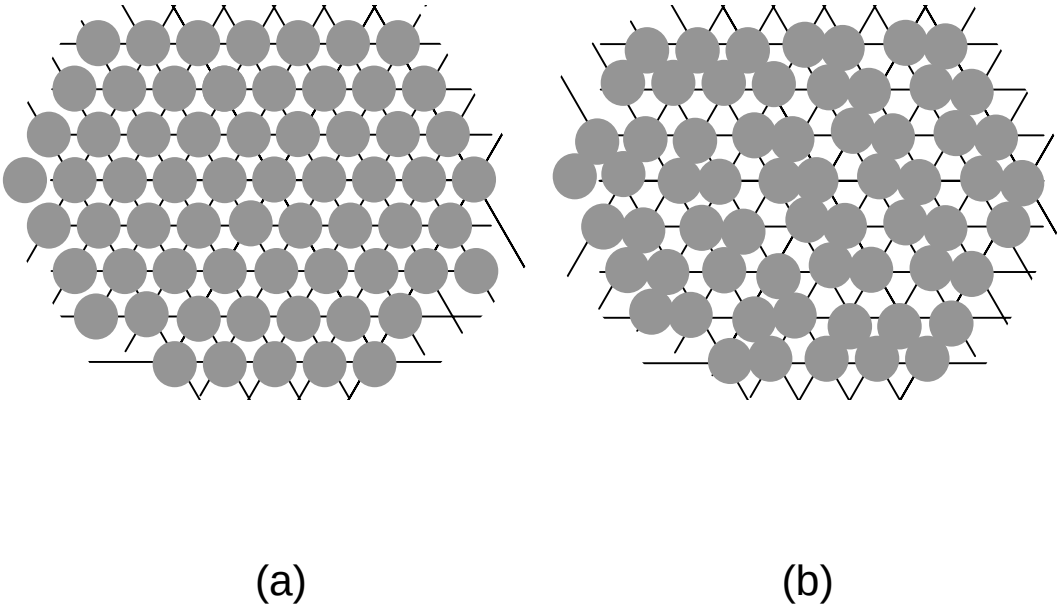

Figure 3.19: Schematics of the two-dimensional structure expected for $Td_{2,3}(C_{12}H_{25})_{16}$ on graphite from a 20 µg/ml solution. (a) In average each dendrimer occupies one site of a hexagonal lattice. (b) Due to the short-range attraction the dendrimers are moving towards one or at most two neighbours.

Bibliography

1) Hooke, R. *Some physiological descriptions of minute bodies made by magnifying glasses* London, 1665.

2) Abbe, E. *Arch. Mikrosk. Anat.* **1873**, *9*, 413.

3) Brune, D.; Hellborg, R.; Whitlow, H.; Hunderi, O. *Surface Characterization*; Wiley-VCH: Weinheim, 1997.

4) Ruska, E. *Z. Phys* **1933**, *83*, 684.

5)Binnig, G.; Rohrer, H.; Gerber, C.; Weibel, E. *Appl. Phys. Lett.* **1982**, *40*, 178.

6)Strong, L.; Whitesides, G. M. *Langmuir* **1988**, *4*, 546-558.

7) Poirier, C. *Chem. Rev.* **1997**, *97*, 1117-1127.

8) Nelles, G.; Schoenherr, H.; Jaschke, M.; Wolf, H.; Schaub, M.; Küther, J.; Tremel, W.; Bamberg, E.; Ringsdorf, H.; Butt, H.-J. *Langmuir* **1998**, *14*, 808-815.

9) Manne, S.; Gaub, H. E. *Science* **1995**, *270*, 1480-1482.

10) Jaschke, M.; Butt, H.-J.; Gaub, H. E.; Manne, S. *Langmuir* **1997**, *13*, 1381-1384.

11) Ducker, W. A.; Wanless, E. J. *Langmuir* **1999**, *15*, 160-168.

12) Rinia, H. A.; Kik, R. A.; Demel, R. A.; Snel, M. M. E.; Killian, J. A.; van der Eerden, J. P. J. M.; de Kruijff, B. *Biochemistry* **2000**, *39*, 5852-5858.

13) Hellmann, J.; Hamano, M.; Karthaus, O.; Ijoro, K.; Shimomura, M.; Irie, M. *Jpn. J. Appl. Phys.* **1998**, *37*, L816-L819.

14) Cui, G.; Xu, Y.; Liu, M.; Fang, F.; Ji., T.; Chen, Y.; Li., Y. *Macromol. Rapid Commun.* **1999**, *20*, 71-76.

15) Stocker, W.; Karakaya, B.; Schürmann, B. L.; Rabe, J. P.; Schlüter, A. D. *J. Am. Chem. Soc.* **1998**, *120*, 7691-7695.

16) Meiners, J. C.; Elbs, H.; Ritzi, A.; Mlynek, J.; Krausch, G. *J. Appl. Phys.* **1996**, *80*, 2224-2227.

17) Binder, K. *Adv. Polymer Sci.* **1999**, *138*, 1-89.

18) Liu, Y.; Zhao, W.; Zheng, X.; King, A.; Singh, A.; Rafailovich, M. H.; Sokolov, J.; Dai, K. H.; Kramer, E. J.; Schwarz, S. A.; Gebizlioglu, O.; Sinha, S. K. *Macromolecules* **1994**, *27*, 4000-4010.

19) Ahrens, H.; Graf, K.; Helm, C. A. *Langmuir* **2001**, *17*, 3113-3115.

20) Ahrens, H.; Baekmark, T. R.; Merkel, R.; Schmitt, J.; Graf, K.; Raiteri, R.; Helm, C. A. *Chem. Phys. Chem. copublished with Angewandte Chemie, Int. Ed.* **2000**, *1*, 101-106.

21) Bhyrappa, P.; Young, J. K.; Moore, J. S.; Suslick, K. S. *J. Am. Chem. Soc.* **1996**, *118*, 5708.

22) Jansen, J. F. G. A.; de Brabander-van den Berg, E. M. M.; Meijer, E. W. *Science* **1994**, *226*, 1226-1229.

23) Sadamoto, R.; Tomoka, N.; Aida, T. *J. Am. Chem. Soc.* **1996**, *118*, 3978-3979.

24) Wells, M.; Crooks, R. M. *J. Am. Chem. Soc.* **1996**, *118*, 3988-3989.

25) Sidorenko, A.; Houphouet-Boigny, C.; Villavincencio, O.; Hashemzadeh, M.; McGrath, D.; Tsukruk, V. *Langmuir* **2000**, *16*, 10569-10572.

26) Binnig, G.; Quate, C. F.; Gerber, C. *Phys. Rev. Lett.* **1986**, *56*, 930-933.

27) Israelachvili, J. N. *Intermolecular and Surface Forces*; 2 ed.; Academic Press: London, 1992.

28) Sheiko, S. S. *Advances in polymer science* **2000**, *151*, 61-174.

29) Zhong, Q.; Innis, D.; Kjoller, K.; Elings, V. B. *Surf. Sci. Lett.* **1993**, *290*, L688-L692.

30) Putman, C. A. J.; Van der Werf, K. O.; De Grooth, B. G.; Van Hulst, N. F.; Greve, J. *Appl. Phys. Lett.* **1994**, *64*, 2454-2456.

31) Putman, C. A. J.; Van der Werf, K.; de Grooth, B. G.; van Hulst, N. F.; Greve, J. *Biophysical Journal* **1994**, *67*, 1749-1753.

32) Burnham, N. A.; Behrend, O. P.; Oulevey, F.; Gremaud, G.; Gallo, P. J.; Gourdon, D.; Dupas, E.; Kulik, A.; Pollock, H. M.; Briggs, G. A. D. *Nanotechnology* **1997**, *8*, 67-75.

33) Radmacher, M.; Tillmann, R. W.; Gaub, H. E. *Biophys. J.* **1993**, *64*, 735-742.

34) Bar, G.; Rubin, S.; Parikh, A.; Swanson, B.; Zawodzinski, T.; Whangbo, M. *Langmuir* **1997**, *13*, 373-377.

35) Magonov, S. N.; Elings, V.; Whangbo, M. H. *Surface Science* **1997**, *375*, L385-L391.

36) Noy, A.; Sanders, C. H.; Vezenov, D. V.; Wong, S. S.; Lieber, C. M. *Langmuir* **1998**, *14*, 1508-1511.

37) Albrecht, T. R.; Quate, C. F. *J. Appl. Phys.* **1987**, *62*, 2599-2602.

38) Pethica, J. B.; Oliver, W. C. *Physica Scripta* **1987**, *T19*, 61.

39) Butt, H. J.; Seifert, E.; Bamberg, E. *J. Phys. Chem.* **1993**, *97*, 7316-7320.

40) Ohnesorge, F.; Binnig, G. *Science* **1993**, *260*, 1451-1456.

41) Magonov, S. N.; Whangbo, M.-H. *Surface analysis with the STM and AFM*; VCH: Weinheim, 1996.

42) Buhleier, E.; Wehner, W.; Vögtle, F. *Synthesis* **1978**, 155-158.

43) Tomalia, D. A.; Baker, H.; Dewald, J. R.; Hall, M.; Kallos, G.; Martin, S.; Roeck, J.; Ryder, J.; Smith, P. *Polym J.* **1985**, *17*, 117-132.

44) Newkome, G. R.; Yao, Z. Q.; Baker, G. R.; Gupta, V. K. *J. Org. Chem.* **1985**, *50*, 2203-2204.

45) Fischer, M.; Vögtle, F. *Angew. Chem. Int. Ed.* **1999**, *38*, 884-905.

46)Newkome, G. R.; Moorefield, C. N.; Vögtle, F. *Dendritic molecules: Concepts, Syntheses, Prespectives*; VHC: Weinheim, 1996.

47) de Gennes, P. G.; Hervet, H. *Phys. Lett.* **1983**, *44*, 351-360.

48) Bosman, A.; Janssen, H.; Meijer, E. *Chem. Rev.* **1999**, *99*, 1665-1688.

49) Weinmann, H.-J.; Ebert, W.; Misselwitz, B.; Radüchel, H.; Schmitt-Willich, H.; Platzek, J. *Eur. Radiol.* **1997**, *7*, 196.

50) Qualmann, B.; Kessels, M.; Musiol, H.; Sierralta, W.; Jungblut , P.; Moroder, L. *Angew. Chem. Int. Ed. Engl.* **1996**, *35*, 909-911.

51) Mansfield, M. L. *Polymer* **1996**, *37*, 3835-3841.

52) Tsukruk, V. V. *Adv. Mater.* **1998**, *10*, 253-257.

53) Sheiko, S. S.; Gauthier, M.; Möller, M. *Macromolecules* **1997**, *30*, 2343-2349.

54) Schlüter, A. D.; Rabe, J. P. *Angew. Chem. Int. Ed.* **2000**, *39*, 864-883.

55) Jackson, C.; Chanzy, H.; Booy, F.; Drake, B.; Tomalia, D.; Bauer, B.; Amis, E. *Macromolecules* **1998**, *31*, 6259-6265.

56) Liu, J. F.; Ducker, W. A. *Langmuir* **2000**, *16*, 3467-3473.

57) Slomkowski, S.; Miksa, B.; Chehimi, M.; Delamar , M.; Cabet-Deliry, E.; Majoral, J.; Caminade, A. *Reactive and functional polymers* **1999**, *41*, 45-47.

58) Tsukruk, V. V.; Rinderspacher, F.; Bliznyuk, V. N. *Langmuir* **1997**, *13*, 2171-2176.

59) Takada, K.; Diaz, D. J.; Abruna, H. D.; Cuadrado, I.; Casado, C.; Alonso, B.; Moran, M.; Losada, J. *J. Am. Chem. Soc.* **1997**, *119*, 10763-10773.

60) Huck, W.; van Veggel, F.; Sheiko, S.; Möller, M.; Reinhoudt, D. *J. Phys. Org. Chem.* **1998**, 540.

61) Morgenroth, F.; Berresheim, A. J.; Wagner, M.; Mullen, K. *Chemical Communications* **1998**, 1139-1140.

62) Wiesler, U.-M.; Berresheim, A. J.; Morgenroth, F.; Lieser, G.; Müllen, K. *Macromolecules* **2001**, *34*, 187-199.

63) Berresheim, A. J.; Müller, M.; Müllen, K. *Chem. Rev.* **1999**, *99*, 1747-1785.

64) Mongin, O.; Gossauer, A. *Tetrahedron Letters* **1996**, *37*, 3825-3828.

65) Weber, E.; Hecker, M.; Koepp, E.; Orlia, W.; Czugler, M.; Csoregh, I. *Journal of the Chemical Society-Perkin Transactions 2* **1988**, 1251-1257.

66) Morgenroth, F.; Kubel, C.; Mullen, K. *Journal of Materials Chemistry* **1997**, *7*, 1207-1211.

67) Brocorens, P.; Zojer, E.; Cornil, J.; Shuai, Z.; Leising, G.; Mullen, K.; Bredas, J. L. *Synthetic Metals* **1999**, *100*, 141-162.

68) Weill, A. *The physics and fabrication of microstructures and microdevices* Berlin, 1986.

69) Nick, L.; Kindermann, A.; Fuhrmann, J. *J. Colloid Polym. Sci.* **1994**, *272*, 367-371.

70) Stange, T. G.; Mathew, R.; Evans, D. F. *Langmuir* **1992**, *8*, 920.

71) Jaschke, M.; Butt, H.-J. *Rev. Sci. Instrum.* **1995**, *66*, 1258-1259.

72) Kittel, C. *Introduction to the solid state physics*; 7 ed.; John Wiley and Sons (WIE):, 1995.

73) Hentschke, R.; Schürmann, B. L.; Rabe, J. P. *J. Chem. Phys.* **1992**, *96*, 6213-6221.

74) Vernov, A.; Steele, W. A. *Langmuir* **1991**, *7*, 3110-3117.

75)Gauß, J. *personal communication* **2000**.

76) Collins, J. B.; Dill, J. D.; Jemmis, E. D.; Apeloig, Y.; Schleyer, P.; Seeger, R.; Pople, J. A. *Journal of the american chemical society* **1976**, *98*, 5419-5427.

77) Röttger, D.; Erker, G. *Angew. Chem. Int. Ed. Engl.* **1997**, *36*, 812-827.

78) Siebert, W.; Gunale, A. *Chem. Soc. Rev.* **1999**, *28*, 367-371.

79) Kratky, O.; Porod, G. *Rec. Trav.Chim.* **1949**, *68*, 1106.

80) Müller, M. *personal communication* **2001**.

81) Tiesler, U.; Schmitz, L.; Ballauff, M. *Mol. Cryst. Liq. Cryst.* **1994**, *254*, 387-394.

82) McGonigal, G. C.; Bernhardt, R. H.; Yeo, Y. H.; Thomson, D. J. **1991**.

83) Vernov, A.; Steele, W. A. *Langmuir* **1991**, *7*, 2817-2820.

84) Stabel, A.; Heinz, R.; Rabe, J. P.; Wegner, G.; Schryver, F. C.; Corens, D.; Dehaen, W.; Süling, C. *J. Phys. Chem.* **1995**, *99*, 8690-8697.

85) Stabel, A.; Heinz, R.; Schryver, F. C.; Rabe, J. P. *J. Phys. Chem.* **1995**, *99*, 505-507.

Acknowledgements

First of all I would like to thanks Prof. Dr. Hans-Jürgen Butt for the theme of the thesis and his continuous interest. He was always available for answering my questions and discussing my numerous doubts. Without his continuous stimulus and support this thesis would be still “under progress”.

Thanks to Dr. Uwe-Martin Wiesler and to Prof. Müllen from the Max Planck Institut (MPI) für Polymerforschung in Mainz for the synthesis of the dendrimers and for their enlightening introductions to these macromolecules.

Thanks to Dr. Diethelm Johannsmann for supervising me during the ellipsometry measurements and Dr. Marcus Müller for his quick and interesting answers to my questions. Several people significantly contributed to the collaboration with the MPI: Christina Hampel, Dörthe Grebel-Koehler and Roland Bauer from AK Müllen, Teresa and Stefi from AK Knoll. It was nice to collaborate with Dr. Uli Jonas and Michael Wind from AK Spiess because of the enthusiasm and knowledge shown in our work.

I would like to thank Dr. Paolo Samori and Prof. Jürgen Rabe from the Humboldt University in Berlin for the scanning tunnelling microscope measurements and for their nice hospitality in Berlin.

Thanks to Brigitte Niesenhaus from my group in Siegen for some of the AFM measurements.

I would like to thank all the people in my group for the friendly atmosphere and for making every moment during the thesis funny and profitable: Volker Franz, Elmar Bonaccurso, Karlheinz Graf, Michael Kappl, Stefan Ecke, Markus Preuß, Henning Müller, Gleb Yakubov, Cristian Mähner and Roberto Raiteri. In particular thank to Elmar Bonaccurso for his patience with my dummy questions about computer programs and for his presence as a friend. Thanks to the new co-workers of the group for the welcome that made the last year in Siegen a pleasing experience: Annelie Schäfer, Brigitte Niesenhaus, Hanne Christian and Peter Rickert.

This thesis would be unreadable without the participation of Prof. Butt, Volker Franz, Karlheinz Graf and Micheal Kappl. Thanks for your contributions!

The first two years in Mainz have been especially nice for me and I would like to thank all the friends that I have met there.

I dedicate this work to my family that always pushed me to desire more and was always on my side. A special thank to Volker for being with me until the last minute of the thesis.